Nonlinear neutrino oscillations in the expanding Universe

V. Alan Kostelecký and Stuart Samuel*

Physics Department, Indiana University, Bloomington, Indiana 47405

(Received 2 August 1993)

We derive the equations that govern neutrino and antineutrino behavior in the early Universe. Results are presented from numerical simulations incorporating nonlinear effects of the neutrino-antineutrino background as well as the leading CP-symmetric and CP-asymmetric terms arising from the interactions with electrons and positrons. A broad spectrum of neutrino and antineutrino behavior is observed, ranging from vacuumlike to smooth. Oscillations exhibiting self-maintained coherence also appear. We identify a variety of neutrino properties arising as a consequence of the nonlinear neutrino self-interactions. The nonlinear effects tend to suppress any CP asymmetry relative to the linear case. An analytical approximation scheme reproducing bulk neutrino behavior is described. We discuss some physical implications of our results.

PACS number(s): 95.30.Cq, 12.15.Ff, 14.60.Pq

I. INTRODUCTION

In the standard cosmological scenario [1], the early Universe at about a tenth of a second consisted principally of a hot gas of photons, electrons, neutrinos, and their antiparticles in approximate thermodynamic equilibrium at a temperature of about 10 MeV. As the Universe expanded and cooled, the neutrino interaction cross sections decreased until, at a temperature of about 2 MeV, the neutrino component of the gas decoupled thermally. Subsequently, the electrons and positrons annihilated, thereby reheating the photons relative to the neutrinos. The annihilation also slightly reheated the electron neutrinos relative to the muon or other neutrinos, resulting in an electron-neutrino excess of about 1% [2,3].

Despite being decoupled from the photons and other leptons, neutrinos influenced nucleosynthesis through neutrino-nucleon interactions until the temperature dropped by about another factor of 2 and attained the "freeze-out" point $T_f \approx 0.7$ MeV where neutrinos ceased to affect the neutron-proton ratio [4,5]. Subsequently, the primary cosmological role for neutrinos came through their contribution to the energy density of the Universe, which controlled the expansion rate. From the moment of decoupling to the present day, neutrinos evolved according to a Fermi-Dirac distribution, modulo distortions at the 1% level due to the electron-positron reheating. A Cosmic Background Explorer– (COBE-) type experiment able to detect the cosmic neutrino relic should therefore reveal a Fermi-Dirac distribution with a 1% distortion at a temperature of about 2 K. Today, there are about 10^8 relic neutrinos per cubic meter.

This canonical picture assumes that the standard electroweak model holds exactly. In particular, neutrinos are taken to be massless, purely left-handed Dirac particles. The known sensitivity of nucleosynthesis to neutrino

types and properties and the likely sensitivity of other potentially measurable quantities, such as the cosmic-neutrino relic [6], dark matter, or large-scale structure, suggests the early Universe can serve as a probe of non-minimal electroweak physics.

In this paper, we consider effects arising in the early Universe from a particular extension of the minimal standard model. We assume the existence of right-handed neutrinos and corresponding neutrino Dirac masses. We suppose that the neutrino masses are small relative to the mean neutrino energy during the relevant time period, so that we work in the neutrino relativistic limit.

New effects can appear in principle as a result of the additional degrees of freedom and also from the possible presence of neutrino oscillations [7]. Since no net flavor change can occur if the numbers of electron and muon neutrinos are equal, oscillations can only play a role in changing the net electron-neutrino excess. Nonetheless, this leaves open the possibility in principle that neutrino oscillations could produce measurable effects on nucleosynthesis or other observable physics [8–12]. A comprehensive analysis of this issue is difficult because the electron-neutrino excess depends on interactions with background fields, including the neutrinos and antineutrinos themselves. As we discuss below, the neutrino-antineutrino background can be the dominant effect. One goal of this paper is the characterization of neutrino and antineutrino behavior in this nonlinear situation.

The nonlinearity of neutrino oscillations in a dense self-interacting neutrino gas has been addressed by several authors [8,13,14]. The correct form of the self-interaction [15,16] and a scheme for treating the analytical complications involved [17] have been developed only recently. In an earlier work [18], we presented the equations governing the neutrino-antineutrino behavior in the early Universe, incorporating the nonlinear effects of the neutrino-antineutrino background as well as dominant and subdominant effects due to electrons and positrons. We also outlined some results of our numerical simulations to study the general behavior of neutrinos and an-

---

*On leave of absence from the City College of New York.

tineutrinos in this system.

The present work extends this analysis and provides a more detailed study of the system. For simplicity, we consider a two-flavor model, taking one neutrino to be ν_e and denoting the other by ν_μ (although the latter could represent ν_τ instead). The corresponding vacuum masses m_1 and m_2 are taken to satisfy $m_1 < m_2$. These choices simplify the parameter space and avoid various complications such as those arising from CP violation in the neutrino mixing matrix. Thus, the CP asymmetry that appears in our analysis has its origin in the small excess of electrons over positrons in the Universe. Similarly, we disregard any differences in the number and energy distributions between the neutrinos and the antineutrinos. As is discussed below, even within these simplifying assumptions, some interesting effects in flavor physics appear. These have their origin in the nonlinear nature of the problem.

The behavior of a particle of energy E and momentum magnitude p propagating in background fields can be described via an index of refraction n, given by $E_{\text{eff}} = np$, where E_{eff} is the effective particle energy including the interaction energy with the background fields. For a single relativistic neutrino of mass m and specified helicity *in vacuo*, $n \approx 1 + m^2/2p^2$. With two flavors each of two helicities and antiparticles included, the refractive index becomes an 8×8 matrix. In the presence of a background of electrons, positrons, neutrinos, and antineutrinos, this matrix is modified by the addition of a term representing an expectation of the interaction Hamiltonian in the background. Since only the left-handed neutrinos and right-handed antineutrinos participate in the weak interactions and since different flavors have different behavior, the early Universe is effectively a birefringent medium for neutrinos and antineutrinos. The self-interactions imply that the birefringence is nonlinear. In effect, this paper characterizes a range of neutrino and antineutrino behavior arising from the nonlinear birefringence.

In Sec. II, we discuss the analytical form of the equations governing neutrino and antineutrino behavior in the early Universe, both in the usual Dirac form and in a density reformulation that we have found more convenient to implement in the simulations. Some details of our numerical methods and more information on our assumptions is provided in Sec. III. The results of the simulations and a description of the general neutrino behavior observed and properties exhibited is given in Sec. IV, along with an analytical approximation scheme for reproducing the gross features of the neutrino behavior. Section IV also includes a separate discussion of the CP asymmetry, which in principle can affect nucleosynthesis or other observable physics. We conclude in Sec. V. For the convenience of the reader, any new phrases or terms we introduce to denote specific neutrino behaviors or properties are written in italics where they appear for the first time.

II. EQUATIONS

In this section, we present the analytical form of the equations we used to describe the behavior of neutrinos in the early Universe. Section II A outlines a derivation of the equations describing neutrino oscillations in background lepton fields. Section II B discusses a reformulation of the results that we have found more useful for numerical work.

A. Oscillation equations

With the standard assumption of spatial homogeneity and isotropy on the scale of the Hubble volume, the early Universe can be described by the Robertson-Walker metric. At times of interest for our analysis, of order one second or greater, any contribution from the intrinsic curvature is negligible. The effective metric then takes the form

$$ds^2 = dt^2 - a^2(t)d\mathbf{x}^2 , \tag{1}$$

where the time dependence of the scale factor $a(t)$ is governed by the Einstein equations. For a radiation-dominated Universe, $a(t) \propto \sqrt{t}$.

As the Universe expands, it cools. The ambient temperature T_γ of the gas, taken as the photon temperature, is related to the scale factor a by $T_\gamma \propto (g_* a^3)^{-1/3}$. The quantity g_* measures the number of effectively massless degrees of freedom. During the radiation-dominated phase, the photon temperature as a function of time is given by

$$T_\gamma = \left[\frac{45}{16\pi^3 G_N g_*} \right]^{1/4} \frac{1}{\sqrt{t}} , \tag{2}$$

where G_N is Newton's gravitational constant. Prior to the neutrino decoupling, $g_* = 10.75$ and the neutrino temperature $T_\nu = T_\gamma$. After decoupling and electron-positron annihilation, $g_* = 3.36$ and $T_\nu \approx (\frac{4}{11})^{1/3} T_\gamma$. The combination of the change in g_* and the photon reheating means that it is approximately correct to use Eq. (2) with $g_* = 10.75$ for the *neutrino* temperature throughout the radiation-dominated era, even after the electron-positron annihilation. In what follows, we denote the neutrino temperature by T for convenience.

The detailed behavior of neutrinos in the early Universe is governed by a Dirac equation appropriate for the Robertson-Walker metric. The main effects arise from the expansion of the scale factor. Intrinsic quantities such as particle number or masses are unaffected by this, but extrinsic ones must be scaled with the comoving volume. For example, number densities scale as a^{-3}, while momenta $\mathbf{p}$ scale as a^{-1}. Since the relation $E^2 = \mathbf{p}^2 + m^2$ holds, the energy of relativistic particles effectively also scales as a^{-1}.

The presence of the non-Minkowski metric also induces several smaller effects that can be neglected for our purposes. For example, the Dirac spin connection has nonvanishing contributions only from terms that contribute proportional to the Hubble constant $H = \dot{a}/a$, which at a temperature of about $T \sim 1$ MeV has a magnitude of order 10^{-22} MeV. This means the spin connection can be safely disregarded for values of the neutrino mass parameters we consider.

We are interested in the weak interactions of neutrinos

with other leptons and with themselves. The effective Hamiltonian governing these processes is a sum of leading terms from charged and neutral current processes:

$$H = H_c + H_n + \cdots , \qquad (3)$$

where the ellipsis represents higher-order terms in the Fermi constant G_F arising from the expansions of the W and Z propagators. In terms of the fields e, μ, ν_e, and ν_μ, respectively, denoting the electron, the muon, the electron neutrino, and the muon neutrino, the explicit form of H_c is

$$H_c = 2\sqrt{2} G_F(\bar{e}_L\gamma^\lambda e_L \bar{\nu}_{eL}\gamma_\lambda\nu_{eL} + \bar{\mu}_L\gamma^\lambda\mu_L\bar{\nu}_{\mu L}\gamma_\lambda\nu_{\mu L}) , \qquad (4)$$

where a superscript L on a fermion denotes the application of the left-handed projector $(1-\gamma_5)/2$. The explicit form of the relevant terms in H_n is

$$H_n = \tfrac{1}{2}\sqrt{2} G_F(\bar{\nu}_{eL}\gamma^\lambda\nu_{eL}\bar{\nu}_{eL}\gamma_\lambda\nu_{eL} + \bar{\nu}_{\mu L}\gamma^\lambda\nu_{\mu L}\bar{\nu}_{\mu L}\gamma_\lambda\nu_{\mu L}$$
$$+ 2\bar{\nu}_{eL}\gamma^\lambda\nu_{eL}\bar{\nu}_{\mu L}\gamma_\lambda\nu_{\mu L}) . \qquad (5)$$

To lowest order in G_F, quadratic contributions to the neutrino effective Hamiltonian H_{eff} arising from the presence of background fields can be obtained by replacing pairs of fields in the interaction Hamiltonian H with expectation values. Spatial homogeneity and isotropy implies that only the timelike component of these four-vector expectations are nonzero. The resulting neutrino effective Hamiltonian including the vacuum-mass terms can be written in terms of a 2×2 matrix $M = M_m + M_b + M_{\text{fd}}$:

$$H_{\text{eff}} = \frac{G_F}{\sqrt{2}}(\bar{\nu}_{eL},\bar{\nu}_{\mu L})(M_m + M_b + M_{\text{fd}})\begin{bmatrix} \nu_{eL} \\ \nu_{\mu L} \end{bmatrix} . \qquad (6)$$

The vacuum-mass contribution M_m is given by

$$M_m = \begin{bmatrix} -\Delta\cos2\theta & \Delta\sin2\theta \\ \Delta\sin2\theta & \Delta\cos2\theta \end{bmatrix} , \qquad (7)$$

where $\Delta = m_2^2 - m_1^2$ is the difference of squares of the vacuum masses, while θ is the vacuum mixing angle between the flavor basis and the mass-eigenstate basis. The background contribution M_b is given as

$$M_b = \gamma^0 \begin{bmatrix} M_{11} & M_{12} \\ M_{21} & M_{22} \end{bmatrix} , \qquad (8)$$

where

$$M_{11} = -M_{22} = 2\langle\bar{e}_L\gamma_0 e_L\rangle + \langle\bar{\nu}_{eL}\gamma_0\nu_{eL}\rangle - \langle\bar{\nu}_{\mu L}\gamma_0\nu_{\mu L}\rangle$$
$$\qquad (9)$$

and

$$M_{12} = 2\langle\bar{\nu}_{\mu L}\gamma_0\nu_{eL}\rangle, \quad M_{21} = 2\langle\bar{\nu}_{eL}\gamma_0\nu_{\mu L}\rangle . \qquad (10)$$

Note that spatial homogeneity implies that $\langle\bar{\nu}_L\gamma_0\nu_L\rangle = n_{\nu_L} - n_{\bar{\nu}_L}$, where n_ν represents a time-dependent but spatially constant neutrino number density. Similarly, the electron expectation is

$$\langle\bar{e}_L\gamma_0 e_L\rangle = n_{e_L^-} - n_{e_L^+} \approx \tfrac{1}{2}(n_{e^-} - n_{e^+}) .$$

Finally, the contribution M_{fd} represents flavor-diagonal terms that are irrelevant for oscillations and are disregarded henceforth. In addition to the latter, we have also omitted contributions from the expectation $\langle\bar{\mu}_L\gamma_0\mu_L\rangle$ because this represents the muon-antimuon number-density difference, which is negligible since the muons annihilate at temperatures at least an order of magnitude greater than those relevant for our study.

Equation (6) suffices for the description, exact to order G_F, of neutrino propagation in the early Universe. Contributions at higher order in G_F appear from two sources. One is higher-order neutrino-background interactions arising directly from the four-point interactions in Eqs. (4) and (5). The other is higher-order terms in the expansion of the W and Z propagators in Eq. (3). Most of these terms are several orders of magnitude smaller than the terms in Eq. (6) during the period of interest. However, the electron-positron number-density difference $\sim\langle\bar{e}_L\gamma_0 e_L\rangle$ is a small quantity. Terms at order G_F^2 that contribute as the sum of the electron-positron number densities could therefore be significant. In fact, such terms exist and give an additional contribution M_a to the matrix M, to be described in Sec. II B below. The numerical analysis discussed in later sections incorporates effects from these terms.

The effective Dirac equation governing the propagation of a left-handed neutrino follows directly from the expression for H_{eff}. The equation is nonlinear due to the presence in H_{eff} of quantities quadratic in the neutrino fields. A complete analysis requires numerical methods. However, it is more effective to reformulate the above equations in terms of density variables. This is the subject of the next subsection.

B. Reformulation

Numerical calculations are more readily performed using number-density variables. Let $v_e^j(t)$ and $v_\mu^j(t)$ denote the flavor components of the neutrino field with energy E^j, with similar expressions for the antineutrino field. We rescale the fields by a volume-dependent factor so that the expression $v_e^{j\dagger}v_e^j + v_\mu^{j\dagger}v_\mu^j$ is a constant independent of time. Since only the excess number of electron neutrinos is relevant for oscillations, we choose this constant for convenience to be equal to the excess-neutrino number N_ν^j (discussed in Sec. III below) at energy E^j in a canonical comoving volume. A similar condition is taken to hold for the antineutrino fields. In what follows, we use the superscript j for neutrinos, k for antineutrinos, and i for both.

The relevant density variables can be incorporated into vectors $\mathbf{v}^j$ and $\mathbf{w}^k$ for neutrinos and antineutrinos, respectively[1]:

---

[1] These vectors play a role analogous to the density matrices $\mathcal{V}^j$ and $\mathcal{W}^k$ of Ref. [18].

$$\mathbf{v}^{j} \equiv (\nu_e^{j\dagger}\nu_e^{j} - \nu_\mu^{j\dagger}\nu_\mu^{j}, 2\,\mathrm{Re}(\nu_e^{j\dagger}\nu_\mu^{j}), 2\,\mathrm{Im}(\nu_e^{j\dagger}\nu_\mu^{j}))\ ,$$

$$\tag{11}$$

$$\mathbf{w}^{k} \equiv (\bar{\nu}_e^{k\dagger}\bar{\nu}_e^{k} - \bar{\nu}_\mu^{k\dagger}\bar{\nu}_\mu^{k}, 2\,\mathrm{Re}(\bar{\nu}_e^{k\dagger}\bar{\nu}_\mu^{k}), 2\,\mathrm{Im}(\bar{\nu}_e^{k\dagger}\bar{\nu}_\mu^{k}))\ .$$

Then, the neutrino-oscillation equations can be rewritten in terms of $\mathbf{v}^{j}$ in a form resembling the motion of a particle in a magnetic field. The same is true for the antineutrino-oscillation equations in terms of $\mathbf{w}^{k}$.

The new equations are[2] [18]

$$\frac{d\mathbf{v}^{j}}{dt} = \mathbf{v}^{j} \times \mathbf{B}_v^{j},\quad \frac{d\mathbf{w}^{k}}{dt} = \mathbf{w}^{k} \times \mathbf{B}_w^{k}\ . \tag{12}$$

The "magnetic" fields $\mathbf{B}_v^{j}$ and $\mathbf{B}_w^{k}$ follow from the equations in the previous subsection. They are given by

$$\mathbf{B}_v^{j} = \frac{\Delta}{2E^{j}} - \mathbf{V}_{vv} - (V_{CP+}^{j} + V_{CP-})\hat{\mathbf{e}}_1\ ,$$

$$\tag{13}$$

$$\mathbf{B}_w^{k} = \frac{\Delta}{2E^{k}} + \mathbf{V}_{vv}^{*} - (V_{CP+}^{k} - V_{CP-})\hat{\mathbf{e}}_1\ .$$

In these equations,

$$\Delta = \Delta(\cos2\theta, -\sin2\theta, 0)$$

and $\hat{\mathbf{e}}_1 = (1, 0, 0)$. The quantities V are effective potentials that arise from the presence of the background fields.

Defining the action of CP as interchanging neutrino and antineutrino fields without sign change, it follows from Sec. II A that the background electrons and positrons create CP-symmetric and CP-asymmetric potentials. These are given by [20]

$$V_{CP+}^{i} = -2\sqrt{2}G_F E^{i}(\rho_{e^-} + p_{e^-} + \rho_{e^+} + p_{e^+})/M_W^2\ , \tag{14}$$

where ρ and p represent energy density and pressure, respectively, and

$$V_{CP-} = \sqrt{2}G_F(n_{e^-} - n_{e^+})\ . \tag{15}$$

The CP-symmetric potential (14) arises from the additional order-G_F^2 contribution M_a to the matrix M of Eq. (6), as mentioned in the previous subsection. Note that higher-order effects in G_F arising from Z exchange are omitted from Eq. (14), since they are approximately 2 orders of magnitude smaller than V_{CP+}^{i} and hence are negligible for the time period during which our simulations are performed.

Similarly, the potential for the neutrino/antineutrino self-interaction is given by

$$\mathbf{V}_{vv} = \frac{\sqrt{2}G_F}{a^3}(\langle \mathbf{v} \rangle - \langle \mathbf{w}^{*} \rangle)\ , \tag{16}$$

where $\langle \mathbf{v} \rangle = \sum_j \mathbf{v}^{j}$ and $\langle \mathbf{w} \rangle = \sum_k \mathbf{w}^{k}$ represent the net background values for the neutrino and antineutrino vectors and $a^3(t)$ has been selected as the canonical comoving volume in our normalization conventions. The conservation of particle number in a comoving volume at fixed energy is expressed in the reformulated equations as

$$\mathbf{v}^{j} \cdot \frac{d\mathbf{v}^{j}}{dt} = 0,\quad \mathbf{w}^{k} \cdot \frac{d\mathbf{w}^{k}}{dt} = 0\ . \tag{17}$$

Note also that Eqs. (15) and (16) are independent of neutrino/antineutrino energy.

In the above equations, we use an asterisk on a vector to indicate a change of sign of the third component. It follows that the vector $\mathbf{w}^{*k}$ obeys the equation

$$\frac{d\mathbf{w}^{*k}}{dt} = \mathbf{w}^{*k} \times \mathbf{B}_{w*}^{k}\ , \tag{18}$$

where $\mathbf{B}_{w*}^{k} = -(\mathbf{B}_w^{k})^{*}$.

The various vector contributions to Eqs. (13) are illustrated in Fig. 1. The four component-vector contributions to $\mathbf{B}_v^{j}$, and the vector $\mathbf{B}_v^{j}$ itself, are shown (not to scale). The reader should note our choice of orientation of the 1-2-3 axes. A similar figure holds for the vector $\mathbf{B}_w^{k}$, but the vector $V_{CP-}\hat{\mathbf{e}}_1$ now points along the positive 1 axis and the nonlinear term $\mathbf{V}_{vv}^{*}$ is reflected in the 1 and 2 axes.

An intuitive understanding of the relative importance of the various terms in Eq. (13) at different times in the early Universe can be found as follows. Associated with each term in the fields $\mathbf{B}$ is an effective oscillation time defined as 2π over the modulus of that term. We denote these oscillation times as τ_{vac}^{i} for the potential involving Δ, τ_{CP+}^{i} for the CP-symmetric potential, τ_{CP-} for the CP-asymmetric potential, and τ_{vv} for the self-interaction potential. The latter is determined by nonlinear dynamics, but it is always larger than the minimum length

$$\tau_{vv}^{min} = 2\pi a^3 / [\sqrt{2}G_F(\langle |\mathbf{v}| \rangle + \langle |\mathbf{w}| \rangle)]\ ,$$

where $\langle |\mathbf{v}| \rangle = \sum_j |\mathbf{v}^{j}|$ and $\langle |\mathbf{w}| \rangle = \sum_k |\mathbf{w}^{k}|$. Note that $\langle |\mathbf{v}| \rangle / a^3$ and $\langle |\mathbf{w}| \rangle / a^3$ represent the excess neutrino and antineutrino number densities, respectively. Comparison of the values of these time scales provides a guide to the dominant effects at any time. Note, in particular, that τ_{vac}^{i} and τ_{CP+}^{i} are energy-dependent quantities.

Figure 2 shows all four time scales as a function of time and temperature in the expanding Universe. We use $\langle \tau_{vac} \rangle$ and $\langle \tau_{CP+} \rangle$ to denote the values of τ_{vac}^{i} and τ_{CP+}^{i} averaged over the energy distributions of excess neutrinos
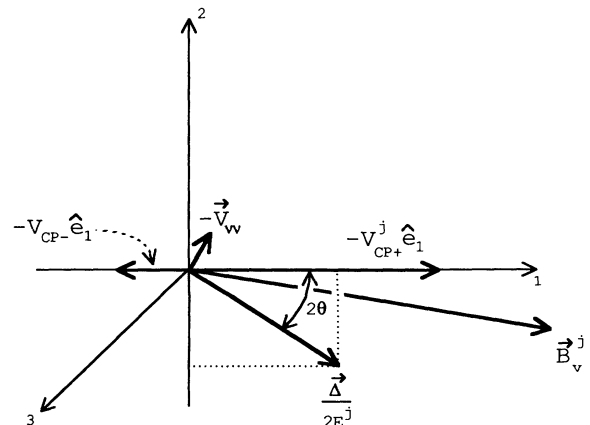
---

[2]Related equations have recently been given in Ref. [19].

FIG. 1. Components of the vector $\mathbf{B}_v^{j}$.

and antineutrinos. A smaller time scale corresponds to a larger and hence more important potential. The inverse Hubble constant $1/H$ is also shown. As a time scale moves above the $1/H$ line, the corresponding term in Eqs. (13) is expected to become unimportant. Note that the CP-asymmetric potential V_{CP-} is relevant only for temperatures above a few tenths of an MeV, and is smaller than V^i_{CP+} for all but the lowest energies E^i.

The figure also displays separately the time scales for electron- and muon-neutrino nonforward scattering, $\langle \tau^{nf}_{\nu_e} \rangle$ and $\langle \tau^{nf}_{\nu_\mu} \rangle$, determined from Ref. [20]. The electron neutrinos interact with electrons somewhat more than the muon neutrinos because of the extra contribution from charged currents. As a consequence, electron neutrinos decouple slightly later than muon neutrinos, as indicated in the figure. This means that electron neutrinos participate more in the reheating due to electron-positron annihilation. The higher temperature results in an excess of ν_e over ν_μ. The associated scales rise above

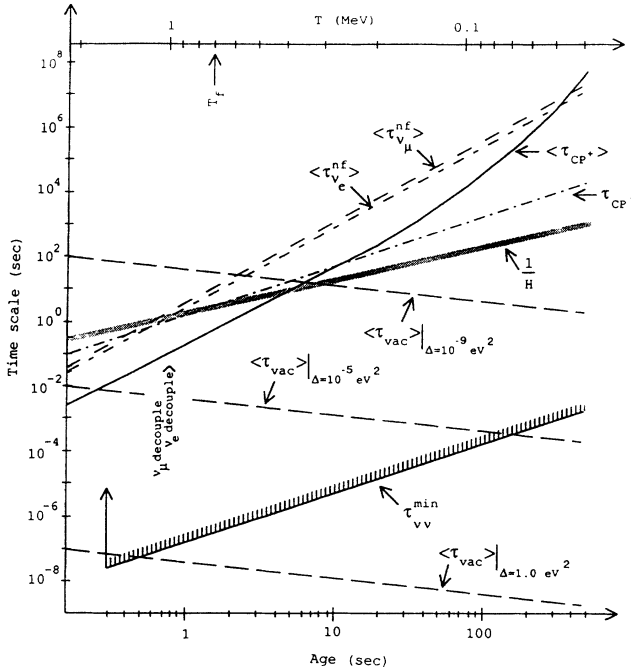FIG. 2. Relevant time scales. Key time scales are displayed as a function of the age t of the Universe. The time scale $\langle \tau_{\text{vac}} \rangle$ is displayed for the cases $\Delta = 10^{-9}$, 10^{-5}, and 1 eV^2. For each factor of 10 increase (or decrease) in Δ, the $\langle \tau_{\text{vac}} \rangle$ line moves down (or up) by one power of ten. The $1/H$ line is drawn with width as a reminder that it acts as an order-of-magnitude estimate of the time at which a scale becomes insignificant. After the temperature of the Universe has dropped below T_f, neutrino flavor effects can no longer influence nucleosynthesis. The average nonforward scattering time scales are plotted separately for ν_e and ν_μ for an average energy of $\bar{E} = 3.151T$. The averages $\langle \tau_{CP+} \rangle$ and $\langle \tau_{\text{vac}} \rangle$ are graphed for an average energy $\bar{E} \approx 5T$. The arrow on the $\tau^{\min}_{\nu\nu}$ line indicates that this quantity becomes effectively infinite at times $t < 0.328$ s, as a result of our step-function approximation for the initial neutrino profile. The hatches on the $\tau^{\min}_{\nu\nu}$ line are a reminder that it provides a lower bound for $\tau_{\nu\nu}$.

the $1/H$ line during the neutrino-decoupling period, and so nonforward scattering subsequently has little effect. This should be contrasted with neutrino forward scattering off electrons, which is relevant until the $\langle \tau_{CP+} \rangle$ line crosses the $1/H$ line at an age of several seconds, and neutrino forward scattering off neutrinos, which is relevant until the $\tau_{\nu\nu}$ line crosses the $1/H$ line. The latter time is determined by the nonlinear dynamics. Since for $\tau^{\min}_{\nu\nu}$ the crossing time is about a million years, the presence of nonlinear effects can mean neutrino forward scattering off neutrinos is relevant long after the time it becomes negligible in the purely linear case.

It is useful to examine the instantaneous fixed points of Eqs. (12), i.e., subsets of the solution space for which the right-hand sides of Eqs. (12) vanish at a given time. For these points, $\mathbf{v}^j$ and $\mathbf{w}^k$ would remain constant in time, were it not for the changes in neutrino/antineutrino energies and backgrounds arising from the expansion of the Universe.

Consider first the simpler case where the nonlinear term is absent and the background potentials are time independent. For a given neutrino energy, the mass matrix M in Eq. (6) can then be diagonalized by a U(2) transformation from the flavor basis to the mass-eigenstate basis. The resulting two mass eigenstates correspond to $\mathbf{v}^j$ aligned along and against $\mathbf{B}^j_v$. These orientations evidently generate fixed points since the cross product vanishes. Analogous statements hold for the antineutrinos. Thus, mass eigenstates correspond to fixed points of Eqs. (12) and, once a neutrino is in a mass eigenstate, it remains so thereafter.

When the nonlinear term is present the determination of fixed points is more difficult. At a fixed point, the vectors $\mathbf{v}^j$ and $\mathbf{w}^k$ must satisfy

$$|\hat{\mathbf{v}}^j \cdot \hat{\mathbf{B}}^j_v| = 1, \quad |\hat{\mathbf{w}}^k \cdot \hat{\mathbf{B}}^k_w| = 1 , \tag{19}$$

where the caret over a quantity denotes a unit vector. However, diagonalization of the matrix M for particles of any one energy changes the background for particles of all other energies and hence can change the alignments of all the other particle vectors. The nonlinearity means that the existence and uniqueness of fixed points is unclear a priori. If Δ, V^i_{CP+} and V_{CP-} are all nonzero, one can argue that any fixed points are isolated by comparing the numbers of equations and constraints. However, if $\Delta = V^i_{CP+} = V_{CP-} = 0$, the system has symmetries leading to continuous families of fixed points. Since, in practice, $\mathbf{V}_{\nu\nu}$ can be much larger than the other potentials, there must be continuous subsets of the solution space that lie close to these families of fixed points. This leads to the notion of approximate nonlinear mass-eigenstate (ANME) configurations. In what follows, we call an ANME configuration any configuration of vectors for which Eqs. (19) are approximately valid. It follows that for ANME configurations the time variations of $\mathbf{v}^j$ and $\mathbf{w}^k$ are relatively slow. Note that, like the linear case, the fixed points are not unique due to the possibility of flipping the signs of $\hat{\mathbf{v}}^j$ and $\hat{\mathbf{w}}^k$.

III. NUMERICAL ANALYSIS

In this section, we discuss some technical details of the numerical analysis and present information about the simulations performed.

We begin with a discussion of the numerical treatment of the energy distributions of the excess neutrinos and antineutrinos. The excess number-density distribution $f_{v_e}(E,T)$ as a function of energy E and temperature T, incorporating the spectral distortion due to the neutrino reheating by electron-position annihilation, is given by [3]

$$f_{v_e}(E,T) \approx (6 \times 10^{-4}) \frac{E}{T} \left[\frac{11E}{4T} - 3 \right] \frac{E^2}{2\pi^2} (e^{E/T} + 1)^{-1} .$$

(20)

This distribution is shown in Fig. 3. Note that a negative value for $f_{v_e}(E,T)$ implies an excess of v_μ.

For programming purposes, the continuous energy variable is approximated by a finite number of bins. We have experimented with both constant and variable energy-bin spacing. A sample choice with 50 energy bins and the corresponding values for the distribution at the temperature 1.5 MeV is shown in Table I. The fourth column is obtained using

$$n_v^j = f_{v_e}(E^j,T)\Delta E^j ,$$

(21)

where E^j is the average density in the bin and ΔE^j is the width of the bin.

For definiteness, we choose the factor $a(t)$ to be 1 MeV^{-1} at the temperature 1.5 MeV. Extrinsic quantities are scaled by the appropriate power of $a(t)$. The norms of $\mathbf{v}^j$ and $\mathbf{w}^k$ are initially equal to the number of excess neutrinos N_v^i with energy E^i in the comoving volume $a^3(t)$, i.e.,
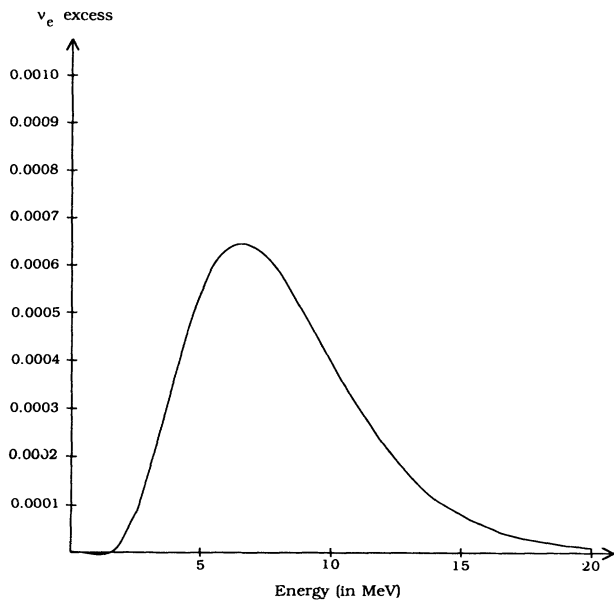
$$N_v^i = \frac{|n_v^i(T=1.5 \text{ MeV})|}{(1 \text{ MeV})^3} .$$

(22)

Since the norms do not change with time, $|\mathbf{v}^i| = |\mathbf{w}^i| = N_v^i$ for all times.

The physical v_e and $\bar{v}_e$ excesses are produced over a

TABLE I. Initialization profile. This table displays the bin number, the average energy in the bin, and the excess-neutrino number density as determined at the temperature $T=1.5$ MeV. The total excess is 4.84×10^{-3} neutrinos per MeV^{-3}.

Bin a	ΔE^j (MeV)	n_v^i (MeV^3)
1	0.0992	-1.4304×10^{-9}
2	0.1555	-5.4916×10^{-9}
3	0.2078	-1.0797×10^{-8}
4	0.2572	-1.9606×10^{-8}
5	0.3068	-3.1671×10^{-8}
6	0.3565	-4.7113×10^{-8}
7	0.4118	-8.1638×10^{-8}
8	0.5914	-7.8583×10^{-7}
9	0.8633	-1.9299×10^{-6}
10	1.6483	-6.4468×10^{-7}
11	2.6393	8.4030×10^{-5}
12	3.2695	1.0596×10^{-4}
13	3.7636	1.5700×10^{-4}
14	4.2595	2.0676×10^{-4}
15	4.7565	2.5026×10^{-4}
16	5.1262	1.3855×10^{-4}
17	5.3759	1.4570×10^{-4}
18	5.6257	1.5144×10^{-4}
19	5.8755	1.5576×10^{-4}
20	6.1002	1.2679×10^{-4}
21	6.3001	1.2798×10^{-4}
22	6.4500	6.4237×10^{-5}
23	6.5500	6.4295×10^{-5}
24	6.7000	1.2847×10^{-4}
25	6.8999	1.2784×10^{-4}
26	7.1247	1.5812×10^{-4}
27	7.3746	1.5540×10^{-4}
28	7.6245	1.5189×10^{-4}
29	7.8744	1.4769×10^{-4}
30	8.1243	1.4293×10^{-4}
31	8.3742	1.3771×10^{-4}
32	8.7462	2.5839×10^{-4}
33	9.2456	2.3435×10^{-4}
34	9.7451	2.0972×10^{-4}
35	10.2446	1.8546×10^{-4}
36	10.7442	1.6228×10^{-4}
37	11.2438	1.4063×10^{-4}
38	11.7435	1.2081×10^{-4}
39	12.2432	1.0297×10^{-4}
40	12.7429	8.7125×10^{-5}
41	13.4701	1.3440×10^{-4}
42	14.4682	9.2789×10^{-5}
43	15.4666	6.2763×10^{-5}
44	16.8591	6.8988×10^{-5}
45	19.3944	4.0387×10^{-5}
46	22.8374	4.3994×10^{-6}
47	25.3284	2.2322×10^{-6}
48	29.2997	2.8185×10^{-7}
49	33.2780	3.2936×10^{-8}
50	37.2611	3.6257×10^{-9}

FIG. 3. Neutrino-excess number-density distribution at $T=1.5$ MeV. At later times, the distribution is the same shape but is scaled.

period of approximately $\frac{1}{2}$ s [2,3]. In the early stages of the production few neutrinos are present, so the nonlinear potential in Eqs. (13) is negligible. These early produced neutrinos start in flavor eigenstates and then begin to oscillate about mean values set by linear mass eigenstates. The oscillation time scale is about 2 orders of magnitude greater than the production time scale. Therefore, neutrinos introduced into the system at different times are out of phase. As more particles are produced, the background grows. Provided that nonlinear effects from this background do not counteract the decoherence, the final neutrino profile is likely to be an ANME configuration.

For the present simulations, we have approximated the continuous production process by an instantaneous one occurring at a temperature of 1.5 MeV ($t \approx 0.328$ s) in ANME configurations. A useful method of constructing these numerically is to begin with analytical mass eigenstates found by setting the terms $\mathbf{V}_{\nu\nu}$ and V_{CP-} to zero (motivation for this is given in Sec. IV D). An iterative procedure with all four potential terms present then can generate ANME configurations satisfying Eqs. (19) to machine accuracy.

To check sensitivity to initial conditions, we have also performed simulations with neutrinos initially in flavor eigenstates. As is discussed in Sec. IV A below, the simulations suggest that neutrino behavior is insensitive to initial conditions for 1 eV$^2 \lesssim \Delta$ and $\Delta \lesssim 10^{-7}$ eV^2. For other values of Δ, initialization in an ANME configuration provides a best guess. However, the reader should be aware that numerical implementation of the physical production mechanism could conceivably generate a different effective initial configuration, such as an ANME configuration rotated slightly toward the flavor axis.

More explicitly, the values of the potentials V_{CP+}^i and V_{CP-} were given according to Eqs. (14) and (15) and are

$$V_{CP+}^i = -\frac{2\sqrt{2}G_F E^i}{M_W^2}\frac{4}{6\pi^2}\int_{m_e}^\infty dE (E^2 - m_e^2)^{1/2}(4E^2 - m_e^2)$$
$$\times (e^{E/T_\gamma}+1)^{-1} \qquad (23)$$

and

$$V_{CP-} = 0.9\eta\frac{2\zeta(3)}{\pi^2}T_\gamma^3 , \qquad (24)$$

where m_e is the electron mass, M_W is the W-boson mass, and the ζ function is $\zeta(3) = 1.20206\ldots$ The integral in Eq. (23) arises from the combination of energy and pressure densities in Eq. (14). In practice, we replaced the full integral with a phenomenological approximation that reproduced values of the integral to the necessary precision. In Eq. (24), the numerical factor of 0.9 represents the percentage of baryons that are protons and hence measures the net excess number of electrons in the Universe. Also, η is the baryon-to-photon ratio, which we took to be 4×10^{-10}. The remaining factors merely count the number of photons at the temperature T_γ. Note that our discussions about neutrino behavior in this paper should be relatively insensitive to numerical uncertainties in parameters such as η or the coefficient

6×10^{-4} in Eq. (20) because the scale for neutrino self-interactions is widely separated from the other scales (cf. Fig. 2).

With N energy bins, Eqs. (12) become a set of $2N$ coupled differential equations. Knowing the initialization profiles, we can then integrate these equations numerically for each energy-bin vector. We used a fourth-order Runge-Kutta method with a variable time step, selected at each step to be several orders of magnitude smaller than the smallest relevant oscillation time at that step.

The simulations were performed on an HP Apollo Series 700 workstation. We studied a region of the $\sin^2 2\theta$-Δ plane given by 10^{-20} eV$^2 < \Delta < 10^2$ eV^2 and $-\pi/2 < 2\theta < +\pi/2$. In particular, we focused on selected values of $\sin^2 2\theta$, including a "medium" value of 0.25 and a "large" value of 0.81. Small values lead to little flavor evolution and are therefore of lesser interest. For the reader who may wish to examine unexplored areas of the plane, the list of values we have studied are listed in Table II.

Previous treatments of neutrino oscillations in the early Universe neglect the terms V_{CP+}^i and $\mathbf{V}_{\nu\nu}$. Under this assumption, a Mikheyev-Smirnov-Wolfenstein- (MSW-) type conversion [21] for neutrinos (but not antineutrinos) occurs for Δ around 10^{-7} eV^2. From Fig. 2, one sees that $\langle \tau_{\text{vac}} \rangle$ and τ_{CP-} cross at $T \sim 1$ MeV, so the vacuum term containing Δ partially cancels the potential V_{CP-} in Eqs. (13). At earlier times V_{CP-} is larger so $\mathbf{B}_v^j$ points almost along $-\hat{\mathbf{e}}_1$, while at later times the vacuum term dominates and $\mathbf{B}_v^j$ points along $\hat{\Delta}$. This means $\mathbf{B}_v^j$ undergoes a large rotation. Provided the rotation is slow relative to the neutrino-oscillation time scale, the neutrino vectors can follow $\mathbf{B}_v^j$, resulting in a large flavor conversion [9]. Our test simulations using only V_{CP-} and the vacuum term containing Δ verify that this occurs.

In contrast, with V_{CP+}^j present only a small neutrino flavor conversion occurs for Δ around 10^{-7} eV^2. The vector $\mathbf{B}_v^j$ undergoes a much smaller rotation because at earlier times it now points almost along $+\hat{\mathbf{e}}_1$ instead of

TABLE II. Runs performed.

Δ (eV^2)	$\sin^2 2\theta$
1.0×10^{-20}	0.25, 0.81
1.0×10^{-15}	0.01, 0.25, 0.81
1.0×10^{-14}	0.81
1.0×10^{-12}	0.25, 0.81
1.0×10^{-10}	0.25, 0.81
5.0×10^{-10}	0.25
1.0×10^{-9}	0.14, 0.18, 0.25, 0.81
2.0×10^{-9}	0.04, 0.10, 0.14, 0.18, 0.25
3.0×10^{-9}	0.14, 0.25
8.0×10^{-9}	0.14
1.0×10^{-8}	0.25, 0.81
1.0×10^{-7}	0.25, 0.81
1.0×10^{-6}	0.25, 0.81
1.0×10^{-5}	0.25, 0.81
1.0×10^{-4}	0.25, 0.81
$1.0 \times 10^{+2}$	0.25, 0.81

$-\hat{e}_1$ since $|V_{CP+}^j| > |V_{CP-}|$. However, for neutrinos with energies less than about 20 times the average energy, $|V_{CP+}^j| < |V_{CP-}|$ and a large flavor conversion can occur at around $T = 1$ MeV if $\Delta/2E^j$ is slightly smaller than the difference $|V_{CP-}| - |V_{CP+}^j|$, i.e., for $\Delta \sim 3 \times 10^{-9}$ eV². Since this *low-energy MSW conversion* has the potential to lead to interesting effects, we have carried out more simulations in this parameter region; cf. Table II.

IV. RESULTS AND DISCUSSION

In this section, we present details of our results and discuss some features we have identified. Section IV A provides an overview of neutrino behavior in different regions of the $\sin^2 2\theta$-Δ plane. We have found that the oscillations obey certain properties, which are described in Sec. IV B. The issues of *CP* asymmetry and its possible consequences are considered in Sec. IV C. Finally, in Sec. IV D we present an analytical approximation scheme for calculating the neutrino and antineutrino density vectors.

A. Overview of neutrino behavior

For convenience in what follows, we identify four regions of the $\sin^2 2\theta$-Δ plane. They are

region 1 (R1): 1 eV² $\lesssim \Delta$;

region 2 (R2): 10^{-5} eV² $\lesssim \Delta \lesssim 1$ eV² ;

region 3 (R3): 10^{-9} eV² $\lesssim \Delta \lesssim 10^{-5}$ eV² ;

region 4 (R4): $\Delta \lesssim 10^{-9}$ eV² .

In R1, the lepton gas is insufficiently dense to have an appreciable effect. The vacuum terms in Eqs. (12) dominate the potentials due to the background fields and so the system behaves in a manner similar to the vacuum case. Any ANME configurations are close to vacuum-mass eigenstates. If the initial neutrino/antineutrino configuration is in flavor eigenstates, then within a few oscillation times decoherence appears and the average vectors $\langle \mathbf{v} \rangle$ and $\langle \mathbf{w} \rangle$ effectively align themselves along the direction $\hat{\Delta}$ of vacuum-mass eigenstates. The point is that the distribution of energies implies a distribution of oscillation times, so even if the neutrinos begin in phase, they soon decohere.

To be more specific, consider the intrinsic ratio

$$\mathbf{r}_v = \langle \mathbf{v} \rangle / \langle |\mathbf{v}| \rangle , \tag{25}$$

where

$$\langle |\mathbf{v}| \rangle = \sum_j |\mathbf{v}^j| = \sum_j N_v^j = N_v$$

and N_v is the total number of neutrinos in the comoving volume. The presence of the denominator ensures that the components of $\mathbf{r}_v$ range between -1 and 1. It also means that uncertainties arising from our approximations and from imprecisely known parameters tend to cancel. Initially, $\mathbf{r}_v \approx (0.9985, 0, 0)$ rather than $(1, 0, 0)$ due to the small muon-neutrino excess at small energies. The asymptotic value of $\mathbf{r}_v$ is
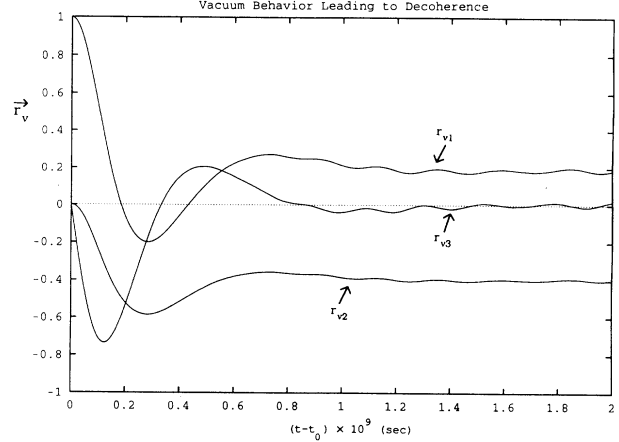

FIG. 4. Vacuum behavior leading to decoherence. The ratios $\mathbf{r}_v$ are displayed as a function of time for $\Delta = 10^2$ eV² and $\sin^2 2\theta = 0.81$.

$$\mathbf{r}_v \approx \cos 2\theta (\cos 2\theta, -\sin 2\theta, 0) .$$

This is readily understood: $\mathbf{r}_v$ points asymptotically along $\hat{\Delta}$. The projection factor of $\cos 2\theta$ is the same as the dot product of the flavor direction $(1, 0, 0)$ and $\hat{\Delta}$. It appears because the vectors $\mathbf{v}^j$ circle around $\hat{\Delta}$ and eventually spread into a cone due to the decoherence.

More generally, if the vectors $\mathbf{v}^j$ initially all point in one direction at an angle α with respect to $\hat{\Delta}$, then asymptotically

$$\mathbf{r}_v \approx \cos \alpha (\cos 2\theta, -\sin 2\theta, 0) .$$

If, instead, the initial vectors form an ANME configuration, then asymptotically $\mathbf{r}_v \approx (\cos 2\theta, -\sin 2\theta, 0)$ because $\cos \alpha \approx 1$.

In analogy with Eq. (25), a ratio $\mathbf{r}_w$ can be defined for the antineutrino vectors. In what follows, our figures do not display $\mathbf{r}_w$ for the nonlinear case because it is indistinguishable from $\mathbf{r}_v$ at the scales used. Also, we often do not show r_{v3} because it is close to zero.

Figure 4 displays $\mathbf{r}_v$ for $\Delta = 10^2$ eV² and $\sin^2 2\theta = 0.81$. Decoherence is apparent after one "bounce." The asymptotic value of $\mathbf{r}_v \approx (0.19, -0.39, 0)$ is achieved.

In R2, neutrino behavior is sensitive to initial conditions. If the initial configuration represents flavor eigenstates, then *self-maintained coherence* [17] arises: a collective mode of the system appears in which some fraction of the particles oscillate in phase.[3] An example of this behavior is shown in Figs. 5 and 6, which display components of the ratio $\mathbf{r}_v$ versus time. Regular periodic behavior occurs, as the neutrino vectors oscillate almost in the 1-2 plane about the direction of the ANME configuration. The neutrino vectors remain bunched together and move more or less as a single unit.

---

[3]The coherence is in flavor space. Quantum decoherence is automatic since the neutrino wave functions have random phases. Note that any overall phase for a neutrino cancels in Eq. (11) and does not affect the oscillations we consider.
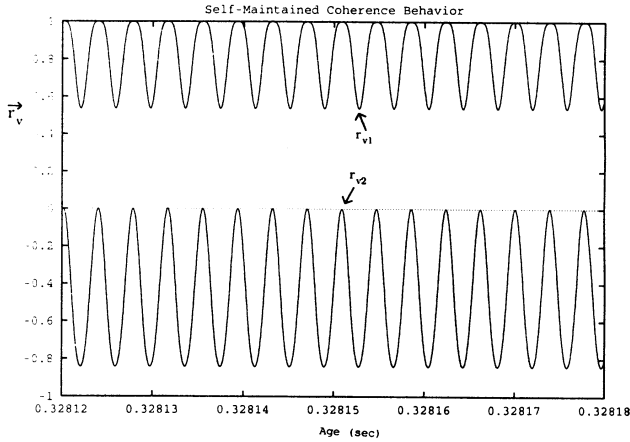
FIG. 5. Self-maintained coherence. The ratios r_{v1} and r_{v2} are displayed as a function of time for $\Delta = 10^{-4}$ eV^2 and $\sin^2 2\theta = 0.25$.

FIG. 7. Disappearance of self-maintained coherence. The small amplitude eventually shrinks to zero.

This behavior can be attributed to the presence of the nonlinear potential term $\mathbf{V}_{vv}$ in the first of Eqs. (13). The motion can be understood via its third component V_{vv3}, proportional to $\langle v_3 \rangle - \langle w_3^* \rangle$. As can be seen from Fig. 6, this quantity periodically changes sign, thereby creating an alternating "magnetic" field along the third direction that induces the back-and-forth planar behavior. The reason why V_{vv3} initially acquires a negative value is discussed below (the "rotation" mechanism). Once this has occurred, the vectors $\mathbf{v}^j$ and $\mathbf{w}^k$ turn toward Δ, eventually overshooting it. At that point, V_{vv3} begins to increase and subsequently turns positive. This then induces the vectors $\mathbf{v}^j$ and $\mathbf{w}^k$ to swing back towards Δ, and the process thereby continues indefinitely. Coherence is maintained, i.e., neutrinos of different energy move together, because V_{vv3} is independent of energy.

For this region of the $\sin^2 2\theta$-Δ plane, any self-maintained coherence eventually disappears when the $\langle \tau_{\text{vac}} \rangle$ line crosses the $\tau_{vv}^{\min}$ line, whereupon the nonlinear term becomes insufficiently strong to maintain coherent behavior. Vacuum behavior then arises instead. This effect is illustrated in Fig. 7. The self-maintained
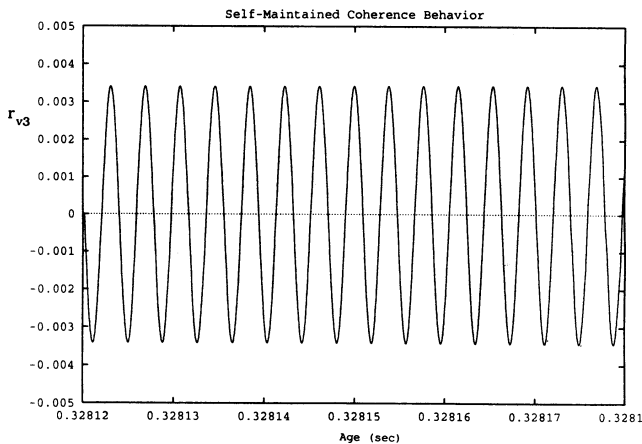

FIG. 6. The ratio r_{v3} as a function of time for $\Delta = 10^{-4}$ eV^2 and $\sin^2 2\theta = 0.25$. Note the relatively small scale of the vertical axis.
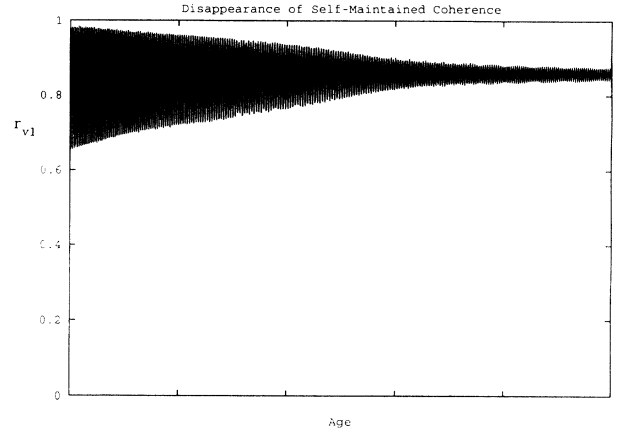
coherent oscillations gradually shrink in amplitude. Lower-energy particles decohere before higher-energy ones, so the process exhibits some continuity. In this particular example, decoherence sets in only after many oscillation times.

If the physical production mechanism leads instead to an effective ANME configuration at our initialization point that is slightly rotated toward the flavor axis, then self-maintained coherence occurs with a smaller amplitude. The general features of this behavior are similar to those discussed above. In what follows, we turn our attention to the case where there is initially an ANME configuration.

In R2, simulations were practical only for $\Delta = 10^{-4}$ and 10^{-5} eV^2. For $\Delta > 10^{-4}$ eV^2 it is desirable to extend the simulation to a time of approximately 6 s, where V_{CP-} and V_{CP+}^i become negligible (cf. Fig. 2). However, at $\Delta = 10^{-4}$ eV^2 this involves more than 10 000 oscillation times, and each tenfold increase in Δ increases the number of oscillation times by an order of magnitude. The buildup of numerical error in the integration algorithm therefore becomes an important issue.

For manageable values of Δ, we observed little motion away from ANME configurations. This held true for several thousand oscillation times. The plots of the three components of $\mathbf{r}_v$ are merely three horizontal lines, so we do not display them. Unless parametric effects arise, the behavior is rather mundane. We also expect this behavior to occur elsewhere in R2, modulo possible parametric effects.

One parametric effect could be self-maintained coherence. Fluctuations in the background may orient some fraction of the particles away from an ANME configuration, thereby inducing small-amplitude self-maintained coherence. Deciding this issue and uncovering any other parametric effects requires more computer power.
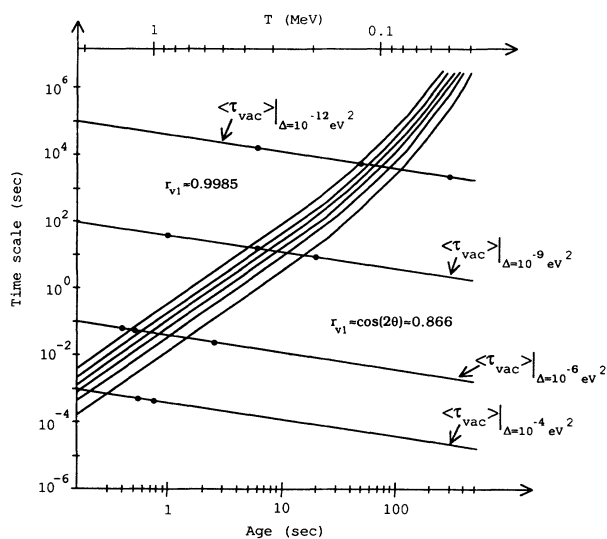
In R3 and R4, the direction of an ANME configuration rotates with time and the particles maintain alignment with it. They begin near flavor eigenstates and smoothly convert to vacuum-mass eigenstates. We refer to this behavior as *evolutionary*. It is achieved by rota-

tion rather than decoherence. The rotation occurs in the region where the $\langle \tau_{\text{vac}} \rangle$ line crosses the $\langle \tau_{CP+} \rangle$ line in Fig. 2.

Figures 8–11 plot lines of constant r_{v1} and r_{v2} for $\sin^2 2\theta = 0.25$ and 0.81. With a fixed value of Δ and the corresponding $\langle \tau_{\text{vac}} \rangle$ line drawn on the figure, the contours provide the values of r_{v1} and r_{v2} at different times. Lines of this type are explicitly drawn on the figures for $\Delta = 10^{-12}$, 10^{-9}, 10^{-6}, and 10^{-4} eV^2. The ratio r_v is near $(1, 0, 0)$ in the upper left of all four figures and becomes $(\cos 2\theta, -\sin 2\theta, 0)$ in the lower right, corresponding to late times for which $\langle \tau_{\text{vac}} \rangle$ drops sufficiently below $\langle \tau_{CP+} \rangle$. The marked points correspond to canonical choices that are listed in Table III; see Sec. IV B. Note that the contour lines are almost parallel to the $\langle \tau_{CP+} \rangle$ line of Fig. 2.
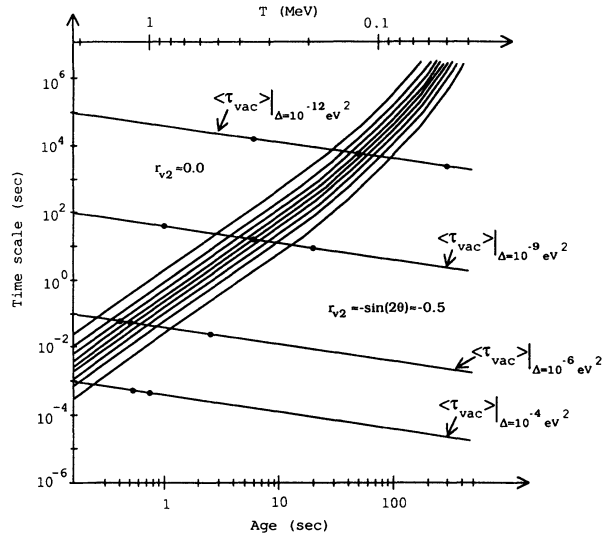
The reasons underlying the evolutionary behavior differ in R3 and R4. In R3, the rotation occurs adiabatically, i.e., any change in the direction of the ANME configurations during an oscillation time is small. To gain insight, it is useful to consider first the linear case, in which $\mathbf{V}_{vv}$ is set to zero and for which the mass eigenstates lie in the 1-2 plane. Simulations for this case also display rotation of the particle vectors from flavor eigenstates to vacuum-mass eigenstates as the region near the $\langle \tau_{CP+} \rangle$ line of Fig. 2 is traversed. The neutrinos and antineutrinos undergo adiabatic rotation, except perhaps for low-energy neutrinos in certain restricted regions of parameter space that convert via an MSW-type effect. Since the various potentials have power-law behavior with time, the relevant time scale for the change in the instantaneous matter-induced mixing angle is the Hubble constant. Hence, as long as the oscillation time is smaller than $1/H$ the motion is adiabatic. As can be seen in Fig. 2, this is true for 10^{-9} eV$^2 \lesssim \Delta$.

Unlike the linear case where a single angle determines

Lines of Constant r_{v2}

FIG. 9. Lines of constant r_{v2} for $\sin^2 2\theta = 0.25$. From top to bottom, the contours displayed are for constant $r_{v2} = -0.05$, -0.10, -0.15, -0.20, -0.25, -0.30, -0.35, -0.40, and -0.45.

the mass eigenstate basis, two angles are needed when the nonlinear term $\mathbf{V}_{vv}$ is present. This is easily seen in our vector reformulation: any ANME configurations are determined by a direction in three-space (cf. Fig. 1). Hence, the definition of adiabaticity used in the linear case must be generalized. One might be tempted to choose as a working definition

$$2\pi \frac{|d\mathbf{B}^i/dt|}{|\mathbf{B}^i|} \ll 1 \tag{26}$$

Lines of Constant r_{v1}

FIG. 8. Lines of constant r_{v1} for $\sin^2 2\theta = 0.25$. From top to bottom, the contours displayed are for constant $r_{v1} = 0.98$, 0.96, 0.94, 0.92, 0.90, and 0.88.
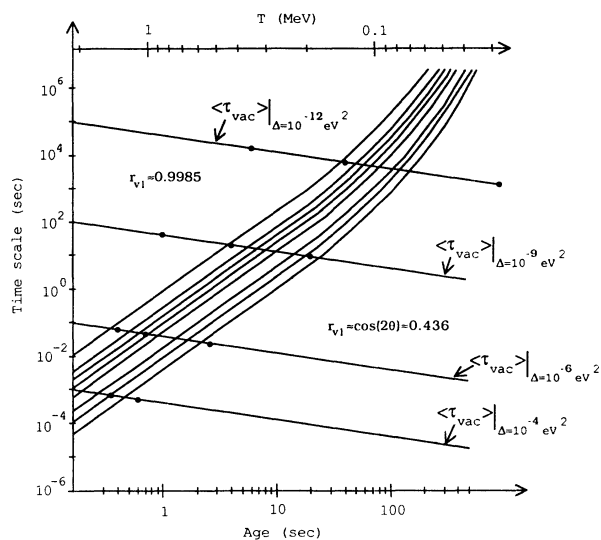

Lines of Constant r_{v1}

FIG. 10. Lines of constant r_{v1} for $\sin^2 2\theta = 0.81$. From top to bottom, the contours displayed are for constant $r_{v1} = 0.98$, 0.9, 0.8, 0.7, 0.6, 0.5, 0.47, and 0.45.
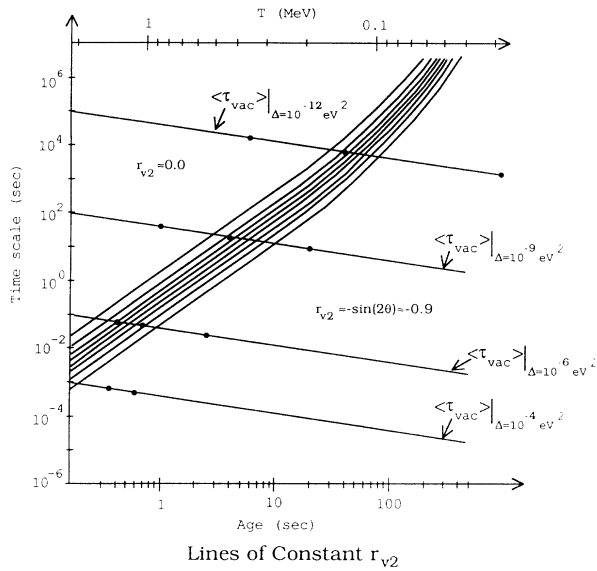
Lines of Constant r_{v2}

FIG. 11. Lines of constant r_{v2} for $\sin^2 2\theta = 0.81$. From top to bottom, the contours displayed are for constant $r_{v2} = -0.1$, -0.2, -0.3, -0.4, -0.5, -0.6, -0.7, and -0.8.

as the adiabaticity condition. When this condition is satisfied, the change of direction of **B** is small during an oscillation time $2\pi/|\mathbf{B}|$, so the particle vectors can follow the motion.

For $\Delta \lesssim 10^{-8}$ eV^2 the behavior of the linear and nonlinear cases is similar. Figure 12 compares the first two components of the ratio $\mathbf{r}_v$ at $\Delta = 10^{-8}$ eV^2. For $\Delta \lesssim 10^{-7}$

TABLE III. Canonical values. This table lists canonical points for the discussion in the text. At $\Delta = 10^{-4}$ eV^2, there is no 4b run because the crossover region is not traversed. The canonical points are marked in Figs. 8–11.

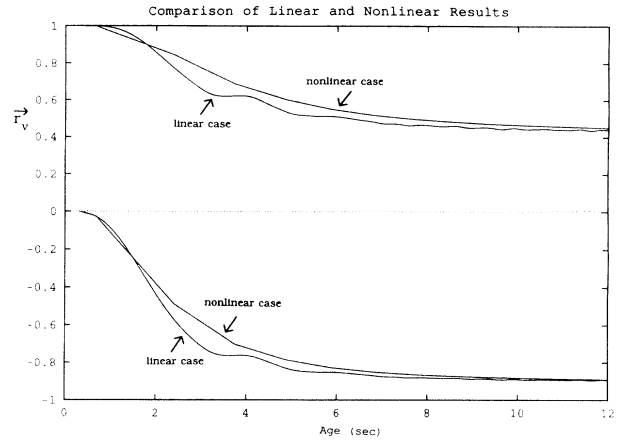| $\sin^2 2\theta$	Point	Δ (eV^2)	Time (s)
0.25	12a	10^{-12}	6.000 47
	12b	10^{-12}	50.001 40
	12c	10^{-12}	300.004 17
	9a	10^{-9}	1.000 00
	9b	10^{-9}	6.000 00
	9c	10^{-9}	20.000 000
	6a	10^{-6}	0.400 00
	6b	10^{-6}	0.511 00
	6c	10^{-6}	2.557 22
	4a	10^{-4}	0.542 39
	4c	10^{-4}	0.763 68
0.81	12a	10^{-12}	6.000 21
	12b	10^{-12}	40.023 32
	12c	10^{-12}	900.003 57
	9a	10^{-9}	1.000 01
	9b	10^{-9}	4.000 05
	9c	10^{-9}	20.000 03
	6a	10^{-6}	0.400 00
	6b	10^{-6}	0.700 00
	6c	10^{-6}	2.692 53
	4a	10^{-4}	0.350 00
	4c	10^{-4}	0.596 65

FIG. 12. Comparison of linear and nonlinear results. The ratios r_{v1} and r_{v2} are displayed as a function of time for $\Delta = 10^{-8}$ eV^2 and $\sin^2 2\theta = 0.81$.

eV^2 the two cases are indistinguishable at this scale. For this reason, we have not used our canonical value of $\Delta = 10^{-6}$ eV^2.

During the simulations with the nonlinear term we checked the condition (26) and found that it was *not* always satisfied. The motion is evidently adiabatic despite this. It turns out that, although the nonlinear term $\langle \mathbf{v} \rangle - \langle \mathbf{w}^* \rangle$ is small, it fluctuates rapidly, thereby inducing violations of the condition (26). However, rapid fluctuations with a tiny amplitude should not ruin adiabaticity. An analogy can be made to the case of an adiabatic MSW effect in the Sun: at distance scales comparable to the electron spacing, an individual neutrino sees a highly fluctuating potential that is small away from the electrons. Nonetheless, adiabaticity is valid. For this reason, we choose to replace Eq. (26) with

$$2\pi \frac{\overline{|d\mathbf{B}^i/dt|}}{|\mathbf{B}^i|} \ll 1 . \tag{27}$$

The bar indicates a time averaging performed over a fraction of an oscillation time. Equation (27) is our definition of the adiabatic condition. In R3 and R4, the neutrino vectors undergo changes in a relatively narrow region called the *crossover region* (see, for example, Figs. 8–11). Over the whole of R3, we found that the condition (27) was satisfied in the crossover region.

In R4 our adiabaticity condition (27) is violated in the crossover region, as expected. Nonetheless, particles exhibit evolutionary behavior from flavor to vacuum-mass eigenstates. However, the transition occurs significantly *before* $\langle \tau_{vac} \rangle$ becomes smaller than $1/H$.

A new type of behavior due to the term $\langle v_3 \rangle - \langle w_3^* \rangle$ is responsible. We call it the *rotation mechanism*, and it works as follows. The vacuum term grows with time, while the other linear potentials V_{CP}^- and $V_{CP^+}^i$ decrease. The direction of an ANME configuration therefore rotates toward Δ, the direction of vacuum-mass eigenstates. However, $\langle \mathbf{v} \rangle$ and $\langle \mathbf{w}^* \rangle$ remain pointing along the flavor axis (1, 0, 0) because all the relevant time scales are initially below the $1/H$ line. From Eqs. (12)

and (18) one sees that eventually $\langle \mathbf{v} \rangle$ begins to acquire a negative third component, while $\langle \mathbf{w}^* \rangle$ acquires a positive one. The net result is a positive contribution to B_3 [cf. Eqs. (13)]. When

$$(\langle v_3 \rangle - \langle w_3^* \rangle)/(\langle |\mathbf{v}| \rangle + \langle |\mathbf{w}| \rangle)$$

becomes

$$\sim -\frac{1}{10} \frac{\tau_{vv}^{min}}{1/H} \; ,$$

$\langle \mathbf{v} \rangle$ and $\langle \mathbf{w}^* \rangle$ begin to rotate toward Δ. Thus, the nonlinear term is found to be responsible for the smooth precocious rotation to vacuum-mass eigenstates.

In Figs. 13 and 14 the linear and nonlinear cases are compared. As anticipated, in the linear case there is no rotation to vacuum-mass eigenstates until the $\langle \tau_{vac} \rangle$ lines crosses the $1/H$ line, whereupon a "bounce" occurs. In contrast, the nonlinear case exhibits evolutionary behavior. Moreover, an examination of individual particle vectors reveals that particles with different energies rotate together, as expected since the nonlinear potential is energy independent.

In Fig. 15 we magnify the time near the crossover region and display the difference of ratios $r_{v3} - r_{w*3}$. It is evident that a buildup of $\sim 10^{-7}$ in these quantities is sufficient to make τ_{vv}^{min} a relevant time scale (cf. Fig. 2), and this is where r_{v1} and r_{v2} begin to change in Figs. 13 and 14.

Finally, we remark that in an area overlapping R3 and R4 near $\Delta = 10^{-9}$ eV^2, both adiabaticity and the rotation mechanism play a role in evolutionary behavior. Figures 16 and 17 display the situation for $\sin^2 2\theta = 0.81$ and 0.25.

B. Neutrino properties

In this subsection, we discuss several properties of neutrino and antineutrino evolution that appear to be generic *in the highly nonlinear regime*, i.e., when $\langle \tau_{vac} \rangle \ll \tau_{vv}^{min}$. We have studied these properties at many points of the $\sin^2 2\theta$-Δ plane. However, to save space we display re-
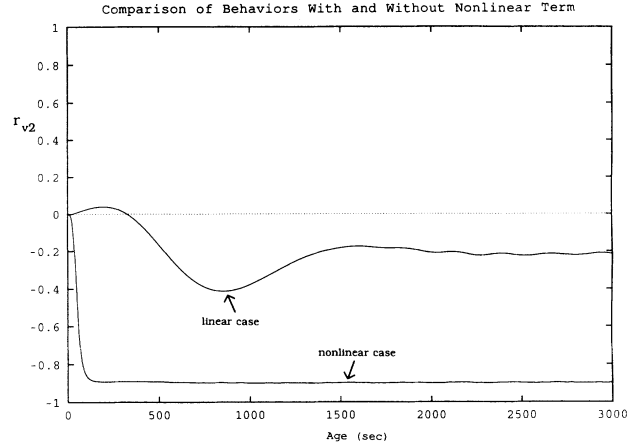

FIG. 14. Comparison of the linear and nonlinear cases. The ratio r_{v2} is shown as a function of time for $\Delta = 10^{-12}$ eV^2 and $\sin^2 2\theta = 0.81$.
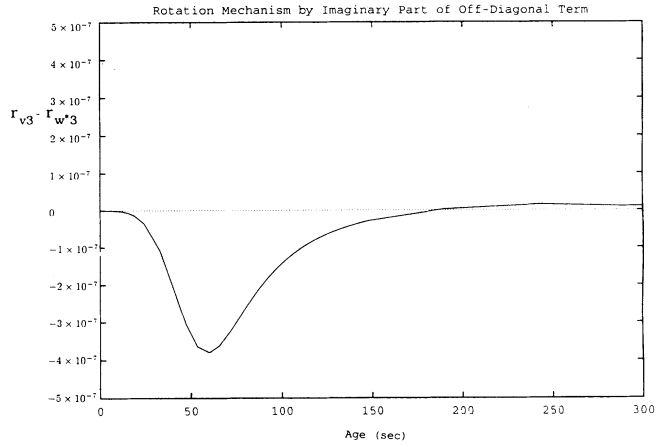

FIG. 15. The rotation mechanism. The difference of ratios $r_{v3} - r_{w*3}$ is displayed as a function of time for $\Delta = 10^{-12}$ eV^2 and $\sin^2 2\theta = 0.81$. Note the magnification of the time scale relative to Fig. 14.
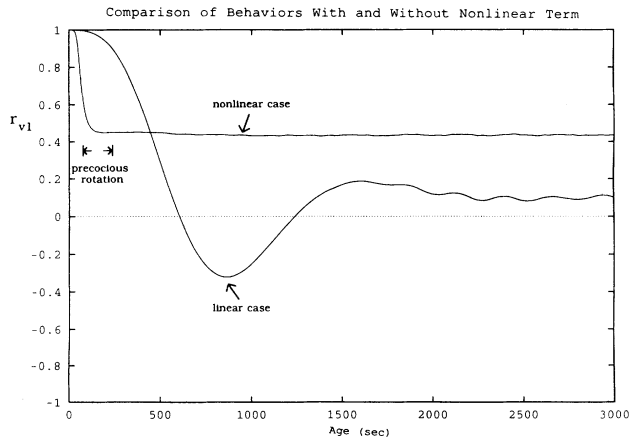

FIG. 13. Comparison of behaviors with and without the nonlinear term. The ratio r_{v1} is shown as a function of time for $\Delta = 10^{-12}$ eV^2 and $\sin^2 2\theta = 0.81$.

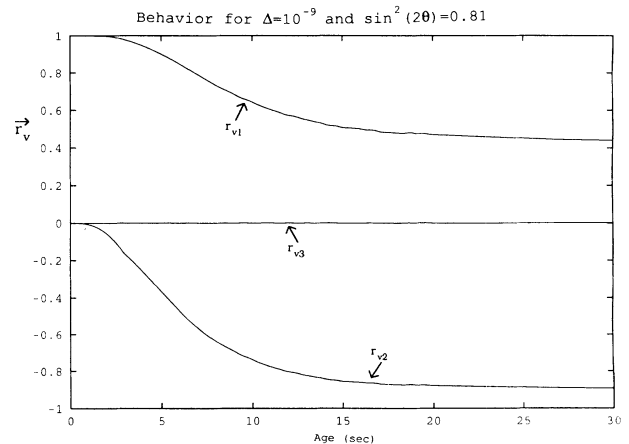FIG. 16. Evolutionary neutrino behavior. The ratios $\mathbf{r}_v$ are displayed as a function of time for $\Delta = 10^{-9}$ eV^2 and $\sin^2 2\theta = 0.81$.
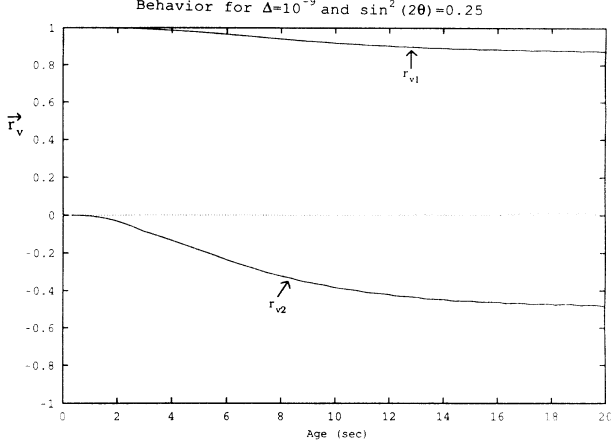
FIG. 17. The ratios r_v as a function of time for $\Delta = 10^{-9}$ eV^2 and $\sin^2 2\theta = 0.25$.

sults here only for the representative values $\Delta = 10^{-4}$, 10^{-6}, 10^{-9}, and 10^{-12} eV^2, and $\sin^2 2\theta = 0.25$ and 0.81. Also, in the tables that follow we consider three characteristic times during a run: an early point a; a point b in the crossover region; and a point c later in the run. The precise times are given in Table III for each of our representative points in the $\sin^2 2\theta$-Δ plane.

The first property we discuss is that particles maintain themselves in ANME configurations after being initialized therein. We call this the *ANME property*. The third column of Table IV displays the average of the test quantity

TABLE IV. Neutrino properties. This table examines some properties of neutrino behavior: the ANME property via t_{ANME}, the related planar quantity via t_p, and the alignment property via t_a.

$\sin^2 2\theta$	Point	t_{ANME}	t_p	t_a
0.25	12a	0.999 998	0.999 999	1.000 000
	12b	0.822 638	0.999 513	0.999 891
	12c	0.999 472	0.999 752	0.999 637
	9a	0.969 034	0.999 647	0.999 974
	9b	0.944 492	0.984 594	0.994 719
	9c	0.997 797	0.997 985	0.999 466
	6a	0.999 991	0.999 996	0.996 300
	6b	0.999 989	0.999 991	0.995 408
	6c	0.999 986	0.999 997	0.999 979
	4a	0.999 998	1.000 000	0.999 984
	4c	0.977 019	0.977 285	0.999 997
0.81	12a	0.999 995	0.999 996	1.000 000
	12b	0.663 304	0.998 458	0.999 782
	12c	0.998 649	0.999 299	0.998 652
	9a	0.999 949	0.999 971	0.999 920
	9b	0.995 491	0.999 560	0.981 697
	9c	0.994 276	0.996 034	0.996 304
	6a	0.999 955	0.999 977	0.981 655
	6b	0.999 947	0.999 976	0.981 630
	6c	0.999 990	0.999 996	0.999 955
	4a	0.999 998	0.999 998	0.999 373
	4c	1.000 000	1.000 000	0.999 970

$$t_{\text{ANME}} = \tfrac{1}{2}(\langle \,|\hat{\mathbf{v}} \cdot \hat{\mathbf{B}}_v|\,\rangle + \langle \,|\hat{\mathbf{w}} \cdot \hat{\mathbf{B}}_w|\,\rangle)\,,\tag{28}$$

where for a quantity Q^i we define

$$\langle Q \rangle = \frac{\sum_i |n_v^i| Q^i}{\sum_i |n_v^i|}\,,\tag{29}$$

where n_v^i is given in Eq. (21). If t_{ANME} is close to one, the particles are in an ANME configuration. By construction, this is initially the case. Fluctuations in the nonlinear background term $\mathbf{V}_{vv}$ tend to cause t_{ANME} to move slowly away from one. Compare, for example, the value of t_{ANME} for $\sin^2 2\theta = 0.25$ at points 4a and 4c. The latter is reached after about 1000 oscillation times.

In R2, the particles start in ANME configurations that are close to vacuum-mass eigenstates and remain close to vacuum-mass eigenstates, provided no parametric effects occur. In R3, particles start in ANME configurations that are near flavor eigenstates and rotate to ones that are approximate vacuum-mass eigenstates. As discussed in the previous subsection, this rotation is adiabatic. As a consequence, the particle vectors can maintain alignment with the effective magnetic fields. Hence, in R2 and R3 it is unsurprising that neutrinos maintain themselves in ANME configurations. We have explicitly checked that for 10^{-8} eV$^2 \lesssim \Delta \lesssim 1$ eV^2 the same property holds in the linear case, as is also to be expected.

If the nonlinear term fails to dominate, so the system is effectively linear, one might anticipate that nonadiabatic rotation would cause vectors to deviate from an ANME configuration and subsequently display other behavior, such as self-maintained coherence. It is instructive to set $\mathbf{V}_{vv}$ to zero. In the linear case at $\Delta = 10^{-12}$ eV^2 and $\sin^2 2\theta = 0.81$, t_{ANME} is less than 0.5 at times after the crossover region. At $\Delta = 10^{-9}$ eV^2 and $\sin^2 2\theta = 0.81$, $t_{\text{ANME}} = 0.86$ beyond the crossover region, which is closer to one because the rotation is closer to being adiabatic. However, the nonlinear case displays robustness in this regard. Although for small Δ the quantity t_{ANME} can be far from unity in the crossover region (cf. the point 12b for $\sin^2 2\theta = 0.81$), it returns close to one at later times.

The reason for this is related to the rotation mechanism discussed in the previous subsection. A significant third component B_3 of the effective magnetic field arises in the crossover region due to the term $\langle v_3 \rangle - \langle w_3^* \rangle$. This creates a mismatch between the particle vectors, which lie almost in the 1-2 plane. To verify this statement, we define a test based on the planar dot product:

$$t_p = \tfrac{1}{2}(\langle \hat{\mathbf{v}}_p \cdot \hat{\mathbf{B}}_{vp} \rangle + \langle \hat{\mathbf{w}}_p \cdot \hat{\mathbf{B}}_{wp} \rangle)\,,\tag{30}$$

where the subscript p indicates that only the first two components of a vector are used. The fourth column in Table IV displays t_p. It is indeed close to one in the crossover region even for small Δ. After passing through the crossover region, an ANME configuration reappears.

Most vectors tend to remain essentially in the 1-2 plane. We call this the *planarity property*. However, there are some exceptions. For example, we have ob-

served low-energy neutrinos undergoing MSW conversion in runs with $\Delta \sim 10^{-9}$ eV^2. The values of r_{v3} and r_{w3} were no bigger than a few times 10^{-2} and usually orders of magnitude smaller.

The planarity property follows from the ANME property because an ANME configuration lies close to the 1-2 plane. In R4, the planarity property is to be expected since the behavior is adiabatic. In the linear case, planarity is also a property of the behavior for 10^{-8} eV$^2 \lesssim \Delta$ because of adiabaticity. For smaller values of Δ in the linear case, the transient oscillatory behavior appearing near the crossover region produces sizable values of r_{v3} and r_{w3} for $\sin^2 2\theta$ sufficiently large. Eventually, decoherence sets in and r_{v3} and r_{w3} become small. However, the third components of individual vectors remain substantial. In contrast, in the full theory with the nonlinear term the average vector and most individual vectors lie almost in the 1-2 plane.

With the exception of low-energy MSW conversions, we have observed that individual vectors are also approximately aligned. We refer to this as the *alignment property*. This concept can be quantified in terms of the average dot product of the individual unit vectors with the unit average vector. We define the alignment test t_a as

$$t_a = \frac{1}{2} \left[\sum_j \mathbf{v}^j \cdot \langle \widehat{\mathbf{v}} \rangle + \sum_k \omega^k \cdot \langle \widehat{\mathbf{w}} \rangle \right]$$

$$\equiv \frac{1}{2} (\widehat{\langle v \rangle} \cdot \langle \widehat{\mathbf{v}} \rangle + \widehat{\langle w \rangle} \cdot \langle \widehat{\mathbf{w}} \rangle) . \qquad (31)$$

The fifth column of Table IV presents values of t_a. These are close to one.

The alignment property can also be explained via the ANME property, since individual ANME configurations for different energy bins are for the most part aligned. This may be contrasted with the linear case. Although alignment holds for 10^{-9} eV$^2 \lesssim \Delta$, for smaller values of Δ the vectors spread after passing through the crossover region. For example, for $\Delta = 10^{-12}$ eV^2 and $\sin^2 2\theta = 0.81$, t_a becomes less than 0.5.

Unlike the ANME property, alignment is also a feature of self-maintained coherence in the highly nonlinear regime. Moreover, alignment holds between the individual neutrino and antineutrino vectors $\mathbf{v}^j$ and $\mathbf{w}^k$. However, this is not true in the linear case in the crossover region and beyond for 10^{-9} eV$^2 \lesssim \Delta$ and sizable mixing angles.

C. CP and the suppression mechanism

In this subsection, we consider effects associated with the CP asymmetry between the neutrino flavors. This is of interest in its own right as well as for physical issues such as nucleosynthesis or neutrino relic detection.

As a measure of CP asymmetry, we define the three quantities

$$CP_\alpha^{asy} = |\langle v_\alpha \rangle - \langle w_\alpha \rangle| / (\langle |\mathbf{v}| \rangle + \langle |\mathbf{w}| \rangle) , \qquad (32)$$

where $\alpha = 1, 2, 3$ labels the three-vector components. The quantity CP_1^{asy} is proportional to the density difference
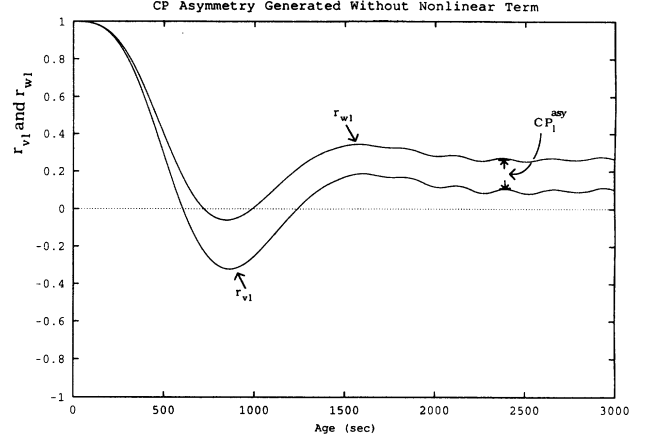

FIG. 18. CP asymmetry in the linear case. The ratios r_{v1} and r_{v2} are shown as a function of time for $\Delta = 10^{-12}$ eV^2 and $\sin^2 2\theta = 0.81$.

between neutrinos and antineutrinos in the flavor basis.[4] When mixing occurs, CP_2^{asy} has a related physical interpretation since the neutrino-antineutrino density difference in the mass-eigenstate basis is proportional to a linear combination of CP_1^{asy} and CP_2^{asy}. It is an open question as to how a sizable CP_3^{asy} could directly affect experiment.

Relative to the linear case, we found that CP asymmetry was suppressed in the full nonlinear system by several orders of magnitude. For the linear case, runs with 10^{-9} eV$^2 \lesssim \Delta$ and $\sin^2 2\theta = 0.81$ produced CP asymmetry of the order of 10%. This substantial accumulation arises throughout R4 because V_{CP-} is larger than V_{CP+}^i in the crossover region. Figure 18 demonstrates that the CP asymmetry is generated in the crossover region. For $\Delta = 10^{-7}$ or 10^{-8} eV^2 and $\sin^2 2\theta = 0.81$, the CP asymmetry was of the order of 1% in the linear case, while for $\Delta \sim 10^{-6}$ eV^2 it was less than 0.0001. For the nonlinear case, the biggest CP asymmetry occurred in CP_3^{asy}. Although it became as big as a few percent in certain runs, it usually was much smaller. The smallness of CP_3^{asy} is aided by the planarity property. In contrast, CP_1^{asy} and CP_2^{asy} were even smaller. Only for selected moments of a few runs did they approach 10^{-4}. Usually they ranged from 10^{-5} to 10^{-7}.

Given the ANME property, we can explain the CP suppression in CP_1^{asy} and CP_2^{asy} as follows. Consider first the linear case. The biggest CP asymmetry occurs when $\mathbf{B}_- = -V_{CP-}\hat{\mathbf{e}}_1$ points in a direction perpendicular to the CP-conserving vector $\mathbf{B}_+ = \Delta/2E - V_{CP+}\hat{\mathbf{e}}_1$ of the other two neutrino potentials. This situation is illustrated schematically in Fig. 19(a), where the neutrino vectors are grouped into an average vector for simplicity. In the

---

[4]Since CP_1^{asy} represents CP asymmetry in the neutrino-antineutrino *excess*, the net CP asymmetry is smaller by about 2 orders of magnitude.

real case, $\mathbf{B}_+$ is energy dependent and the directions of $\mathbf{B}_v = \mathbf{B}_+ + \mathbf{B}_-$ and its analogue $\mathbf{B}_{w^*} = -\mathbf{B}_+ + \mathbf{B}_-$ vary from bin to bin. Note also that $\sqrt{2}G_F\langle\mathbf{v}\rangle/a^3$ and $\sqrt{2}G_F\langle\mathbf{w}^*\rangle/a^3$ are not drawn to scale: these vectors are about 10^7 times longer than $\mathbf{B}_-$ and at least 10^6 times longer than $\mathbf{B}_+$. Their difference is the contribution to the background field. Assuming that the particles are in ANME configurations and using similar triangles, the figure shows that the CP asymmetry should be of order $|\mathbf{B}_-|/|\mathbf{B}_+|$. This agrees in order of magnitude with the CP asymmetry observed in our simulations of the linear case.

When the nonlinear term is also included, the vectors shown in Fig. 19(a) no longer form an ANME configuration because $\mathbf{B}_{vv} \equiv -\mathbf{V}_{vv}$ adds a significant contribution to $\mathbf{B}_v$ and $\mathbf{B}_{w^*}$. In this situation, an ANME configuration requires $\langle\mathbf{v}\rangle$ and $\langle\mathbf{w}^*\rangle$ to be approximately aligned. Figure 19(b) displays the configuration for the nonlinear case. Then, it follows that

$$\frac{|\mathbf{B}_-| - |\mathbf{V}_{vv}|}{|\mathbf{B}_-| + |\mathbf{V}_{vv}|} \approx \frac{a^3|\mathbf{B}_+|}{2\sqrt{2}G_F|\langle\mathbf{v}\rangle|} . \tag{33}$$

Then, the vectors $\mathbf{B}_v = \mathbf{B}_+ + \mathbf{B}_- + \mathbf{B}_{vv}$ and $\mathbf{B}_{w^*} = -\mathbf{B}_+ + \mathbf{B}_- + \mathbf{B}_{vv}$ point almost along $\mathbf{B}_+$. These two vectors are not shown to avoid cluttering the figure. It can be seen that CP_1^{asy} and CP_2^{asy} are of order

$$\frac{a^3|\mathbf{B}_{vv}|}{2\sqrt{2}G_F|\langle\mathbf{v}\rangle|} \approx \frac{a^3|\mathbf{B}_-|}{2\sqrt{2}G_F|\langle\mathbf{v}\rangle|} \approx 10^{-7} . \tag{34}$$

Allowing for the fact that CP suppression should be somewhat larger than this for ANME configurations, this agrees with what we observe numerically.

The above argument also holds if the CP asymmetry is generated by only a few individual neutrino vectors. For example, in runs with $\Delta = 10^{-9}$ eV^2 low-energy neutrinos are MSW rotated whereas antineutrinos remain unaffected. The fraction of neutrinos with low-enough energy for conversion is 3×10^{-4}, so the MSW rotation

generates a $\mathbf{B}_-$ no larger than a factor of 3×10^{-4} of $2\sqrt{2}G_F|\langle\mathbf{v}\rangle|/a^3$. However, the neutrinos and antineutrinos vectors react to maintain ANME configurations and so the observed CP asymmetry is much smaller.

This CP suppression mechanism does not directly apply to CP_3^{asy}. However, it does apply to a similar-seeming but different quantity

$$|\langle v_3\rangle - \langle w_3^*\rangle|/(\langle|\mathbf{v}|\rangle + \langle|\mathbf{w}|\rangle) .$$

Simulations show this quantity is indeed suppressed relative to CP_3^{asy}. This provides additional support for our explanation of the CP suppression. Moreover, our argument also provides a reason why the background ratio

$$|\langle\mathbf{v}\rangle - \langle\mathbf{w}^*\rangle|/(\langle|\mathbf{v}|\rangle + \langle|\mathbf{w}|\rangle)$$

tends to be small, usually ranging from 10^{-5} to 10^{-7} except at times before the crossover region where it is even smaller.

The reader should note that a larger CP asymmetry might arise from parametric effects. Although this does not appear in any of our present data, including those over thousands of oscillation times, a relatively large CP asymmetry could, in principle, accumulate over much longer time scales.

The CP asymmetry we have seen is several orders of magnitude smaller than that reported in Ref. [9] for $\Delta \sim 10^{-7}$ eV^2 where two dominant effects, V_{CP+}^i and $\mathbf{V}_{vv}$, were disregarded. Our results suggest that in the early Universe a very small CP asymmetry is likely to be maintained through much of the critical period when neutrinos could affect nucleosynthesis. If true, CP-asymmetry effects are minimal. The major effect arises from the flavor-excess distortions, implying a shift in the ^{4}He abundance of $\Delta Y \sim (1-2)\times10^{-4}$ [2,3,9].

Another consequence of the CP suppression is an increase in the difficulty of detecting the relic neutrino background. Assuming no unexpected parametric effects, techniques dependent on forward scattering [22] may be impractical.

D. Approximation scheme for particle vectors

Combining the ANME property with the argument for CP suppression in the previous subsection demonstrates that, to a good approximation, the component of $\mathbf{B}_-$ that is *not* aligned along $\mathbf{B}_+$ cancels with the nonlinear term $\mathbf{V}_{vv}$. This suggests that mass eigenstates determined solely from V_{CP+}^i and $\Delta/2E^i$, i.e., $\mathbf{B}_+$ in Fig. 19, should be ANME configurations. It then follows that $\mathbf{v}^j$ and $\mathbf{w}^{*k}$ should be well approximated by calculations involving only these terms.

The energy dependence in V_{CP+}^j implies the existence of a different $\mathbf{B}_+^j$ for each neutrino vector. The same holds for the analogous formulas for antineutrinos. The evolutionary behavior implies $\mathbf{v}^j$ and $\mathbf{w}^{*k}$ should be rotated onto $\mathbf{B}_+^i$ rather than projected. The only ambiguity is whether the $\mathbf{v}^j$ and $\mathbf{w}^{*k}$ point along or against $\hat{\mathbf{B}}_+^i$. The natural choice is to minimize the vector rotation. With this approach, we obtain an analytical approximation given by
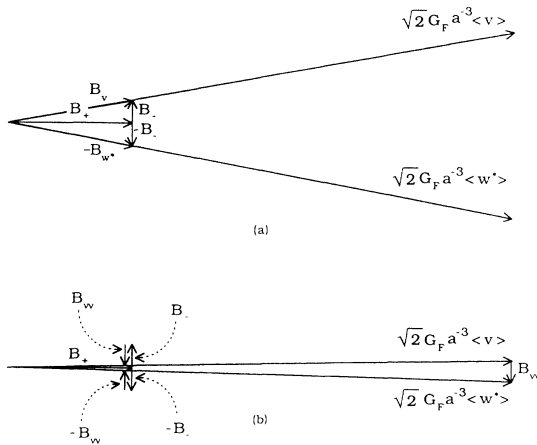

FIG. 19. (a) Vector diagram for estimating CP asymmetry in the linear case. (b) Vector diagram for estimating CP asymmetry in the nonlinear case, under the assumption that particles are in ANME configurations.

TABLE V. Comparison of approximation with simulation: average vectors.

$\sin^2 2\theta$	Point	v_1 (simul.)	v_1 (approx.)	v_2 (simul.)	v_2 (approx.)
0.25	12a	0.998 53	0.998 53	−0.000 50	−0.000 56
	12b	0.975 10	0.969 78	−0.214 64	−0.218 51
	12c	0.869 00	0.864 96	−0.491 19	−0.498 91
	9a	0.998 52	0.998 53	−0.004 46	−0.004 28
	9b	0.965 15	0.965 58	−0.236 62	−0.235 97
	9c	0.873 81	0.875 12	−0.482 80	−0.480 58
	6a	0.981 98	0.981 98	−0.159 93	−0.159 93
	6b	0.965 16	0.965 15	−0.237 67	−0.237 68
	6c	0.868 00	0.867 89	−0.493 58	−0.493 76
	4a	0.868 00	0.868 04	−0.493 56	−0.493 50
	4c	0.866 50	0.865 95	−0.496 19	−0.497 18
0.81	12a	0.998 53	0.998 53	−0.000 92	−0.001 00
	12b	0.967 49	0.943 93	−0.246 34	−0.275 35
	12c	0.433 90	0.435 25	−0.898 04	−0.898 68
	9a	0.998 49	0.998 54	−0.008 10	−0.007 74
	9b	0.945 08	0.948 29	−0.262 78	−0.263 86
	9c	0.469 75	0.470 46	−0.877 67	−0.880 63
	6a	0.926 68	0.926 68	−0.320 62	−0.320 62
	6b	0.714 05	0.714 10	−0.671 58	−0.671 69
	6c	0.443 78	0.444 10	−0.894 46	−0.894 29
	4a	0.473 77	0.473 77	−0.878 27	−0.878 27
	4c	0.443 40	0.443 40	−0.894 65	−0.894 65

$$\mathbf{v}^i = \mathbf{w}^{*i} = \pm N_v^i \hat{\mathbf{B}}_+^i . \tag{35}$$

Our approximation gives zero CP_α^{asy} and zero third components v_3^j and w_3^{*k}. It thereby implements extreme versions of the planarity and CP-suppression properties. Table V presents a comparison of results from the full simulation with numerical values given by the approximation. The first two components of $\langle \mathbf{v} \rangle$ are shown at the canonical points in the $\sin^2 2\theta$-Δ plane. Overall, there is agreement to roughly three decimal places. The biggest difference occurs in the crossover region for small Δ; cf. point 12b, where about two decimal places are reproduced.

TABLE VI. Comparison of approximation with simulation: individual neutrino vectors.

Bin	v_1 (simul.)	v_1 (approx.)	v_2 (simul.)	v_2 (approx.)	v_3 (simul.)
2	0.000 04	−0.000 02	−0.000 03	0.000 05	0.000 02
4	0.000 04	−0.000 09	−0.000 15	0.000 18	−0.000 12
6	0.000 25	−0.000 21	−0.000 25	0.000 42	−0.000 31
8	0.005 66	−0.003 56	−0.001 24	0.007 01	−0.005 31
10	−0.004 02	−0.003 56	0.004 45	0.005 37	−0.002 36
12	0.764 07	0.810 68	−0.720 32	−0.682 34	−0.141 92
14	1.765 85	1.776 35	−1.059 57	−1.058 10	−0.184 68
16	1.263 34	1.262 70	−0.565 39	−0.570 24	−0.062 49
18	1.412 71	1.411 15	−0.544 27	−0.549 54	−0.036 96
20	1.201 44	1.200 09	−0.404 85	−0.409 00	−0.010 78
22	0.614 21	0.613 52	−0.188 08	−0.190 34	0.001 23
24	1.234 92	1.233 62	−0.354 03	−0.358 65	0.009 49
26	1.531 03	1.529 81	−0.394 30	−0.399 83	0.025 59
28	1.480 61	1.479 63	−0.337 00	−0.343 18	0.036 10
30	1.400 33	1.399 61	−0.283 22	−0.289 79	0.042 08
32	2.543 57	2.542 54	−0.446 27	−0.460 57	0.087 81
34	2.075 07	2.074 46	−0.293 51	−0.307 94	0.078 39
36	1.610 81	1.610 48	−0.186 81	−0.199 21	0.061 07
38	1.201 72	1.201 58	−0.116 41	−0.125 64	0.043 71
40	0.867 80	0.867 78	−0.071 62	−0.077 66	0.029 59
42	0.925 49	0.925 62	−0.060 76	−0.064 89	0.027 72
44	0.688 70	0.688 95	−0.036 18	−0.035 89	0.017 83
46	0.043 95	0.043 98	−0.001 62	−0.001 26	0.001 17
48	0.002 82	0.002 82	−0.000 06	−0.000 05	0.000 08
50	0.000 04	0.000 04	0.0	0.0	0.0

TABLE VII. Comparisons of approximation with simulation: individual antineutrino vectors.

Bin	v_1 (simul.)	v_1 (approx.)	v_2 (simul.)	v_2 (approx.)	v_3 (simul.)
2	−0.000 03	−0.000 02	0.000 04	0.000 05	−0.000 02
4	−0.000 08	−0.000 09	0.000 18	0.000 18	0.000 03
6	−0.000 20	−0.000 21	0.000 42	0.000 42	0.000 08
8	−0.002 57	−0.003 56	0.007 38	0.007 01	0.000 84
10	−0.001 98	−0.003 56	0.006 06	0.005 37	0.000 97
12	0.764 30	0.810 68	−0.720 53	−0.682 34	0.139 61
14	1.767 19	1.776 35	−1.061 32	−1.058 10	0.160 19
16	1.265 70	1.262 70	−0.561 45	−0.570 24	0.048 75
18	1.415 16	1.411 15	−0.538 54	−0.549 54	0.025 51
20	1.203 11	1.200 09	−0.399 99	−0.409 00	0.003 89
22	0.614 85	0.613 52	−0.185 96	−0.190 34	−0.003 23
24	1.235 95	1.233 62	−0.350 31	−0.358 65	−0.012 70
26	1.532 03	1.529 81	−0.390 33	−0.399 83	−0.026 45
28	1.481 11	1.479 63	−0.334 95	−0.343 18	−0.034 52
30	1.400 51	1.399 61	−0.282 78	−0.289 79	−0.038 65
32	2.543 31	2.542 54	−0.449 42	−0.460 57	−0.079 02
34	2.074 34	2.074 46	−0.300 77	−0.307 94	−0.069 92
36	1.610 03	1.610 48	−0.195 24	−0.199 21	−0.054 93
38	1.201 07	1.201 58	−0.124 10	−0.125 64	−0.040 04
40	0.867 33	0.867 78	−0.077 76	−0.077 66	−0.027 78
42	0.925 02	0.925 62	−0.067 57	−0.064 89	−0.027 45
44	0.688 43	0.688 95	−0.040 52	−0.035 89	−0.019 01
46	0.043 94	0.043 98	−0.001 74	−0.001 26	−0.001 28
48	0.002 82	0.002 82	−0.000 06	−0.000 05	−0.000 09
50	0.000 04	0.000 04	0.0	0.0	0.0

The approximation works best for large Δ at early times, away from the crossover region. Tables VI and VII contain the comparison for individual neutrino and antineutrino vectors, respectively, for $\sin^2 2\theta = 0.81$ at the point 9b. To save space, only every other bin is shown for a 50-bin division of the energy spectrum. Also, we have not shown the approximation for v_3^j or w_3^{*k} since they are always zero. The true numbers are 10^{-4} times the ones displayed. In most bins there is three-figure agreement. The approximation is better for higher-energy bins because V_{CP+}^i is relatively more important than V_{CP-} there. This should be contrasted with the lowest-energy vectors, for which even the sign is incorrect. Point 9b was specially selected to illustrate this effect. The low-energy neutrinos have undergone MSW conversion and hence are pointing approximately in the opposite direction to the others. Note that the corresponding low-energy antineutrinos have *not* undergone MSW conversion and so there is better agreement.

V. CONCLUSION

In this paper, we have derived equations governing neutrino and antineutrino behaviors in the early Universe and have presented results from numerical simulations. The analysis incorporates the nonlinear effects of the neutrino-antineutrino background as well as leading CP symmetric and CP asymmetric terms arising from the interactions with electrons and positrons.

The observed behaviors of neutrinos and antineutrinos depend on the values of $\sin^2 2\theta$ and Δ. The behavior ranges from vacuumlike at relatively large values of Δ to evolutionary or to oscillations exhibiting self-maintained coherence. Several neutrino properties arising from the nonlinear neutrino self-interactions can be identified, including maintenance in ANME configurations, planarity, and alignment. The nonlinear effects tend to suppress any CP asymmetry relative to the linear case. We have also presented an analytical approximation scheme for particle densities.

In the absence of possible parametric effects such as self-maintained coherence, the CP suppression mechanism suggests that the effect of the flavor excess on nucleosynthesis is minimal. It also implies that the cosmic-neutrino relic may be more difficult to detect than expected. In contrast, if self-maintained coherence is realized in nature one can speculate about more striking effects, including consequences for dark matter and for the large-scale structure of the Universe.

ACKNOWLEDGMENTS

[1] See, for example, E. W. Kolb and M. S. Turner, *The Early Universe* (Addison Wesley, Redwood City, CA, 1990).

[2] S. Dodelson and M. S. Turner, Phys. Rev. D **46**, 3372 (1992); B. Fields, S. Dodelson, and M. S. Turner *ibid.* **47**, 4309 (1993).

[3] A. D. Dolgov and M. Fukugita, Phys. Rev. D **46**, 5378 (1992).

[4] T. P. Walker, G. Steigman, D. N. Schramm, K. A. Olive, and H. S. Kang, Astrophys. J. **376**, 51 (1991).

[5] K. A. Olive, D. N. Schramm, D. Thomas, and T. P. Walker, Phys. Lett. B **265**, 239 (1991).

[6] For reviews, see, for example, P. F. Smith, in *Trends in Astroparticle Physics*, edited by D. B. Cline and R. Peccei (World Scientific, Singapore, 1990); P. F. Smith and J. D. Lewin, Phys. Rep. **187**, 203 (1990).

[7] For a review, see, for example, T. K. Kuo and J. Pantaleone, Rev. Mod. Phys. **61**, 937 (1989).

[8] A. D. Dolgov, Yad. Fiz. **33**, 1309 (1981) [Sov. J. Nucl. Phys. **33**, 700 (1981)].

[9] P. Langacker, S. T. Petcov, G. Steigman, and S. Toshev, Nucl. Phys. **B282**, 589 (1987).

[10] M. J. Savage, R. A. Malaney, and G. M. Fuller, Astrophys. J. **368**, 1 (1991).

[11] K. Enqvist, K. Kainulainen, and J. Maalampi, Nucl. Phys. **B349**, 754 (1991).

[12] X. Shi, D. N. Schramm, and B. D. Fields, University of Chicago Report, 1993 (unpublished).

[13] L. Stodolsky, Phys. Rev. D **36**, 2273 (1987).

[14] M. J. Thomson and B. McKellar, Phys. Lett. B **259**, 113 (1991).

[15] J. Pantaleone, Phys. Lett. B **287**, 128 (1992).

[16] J. Pantaleone, Phys. Rev. D **46**, 510 (1992).

[17] S. Samuel, Phys. Rev. D **48**, 1462 (1993).

[18] V. A. Kostelecký, J. Pantaleone, and S. Samuel, Phys. Lett. B **315**, 46 (1993).

[19] G. Sigl and G. Raffelt, Max-Planck Institute Report No. MPI-Ph/92-112 (unpublished).

[20] D. Notzold and G. Raffelt, Nucl. Phys. **B307**, 924 (1988).

[21] L. Wolfenstein, Phys. Rev. D **17**, 2369 (1978); **20**, 2634 (1979); S. P. Mikheyev and A. Yu. Smirnov, Yad. Fiz. **42**, 1441 (1985) [Sov. J. Nucl. Phys. **42**, 913 (1985)]; Usp. Fiz. Nauk **153**, 3 (1987) [Sov. Phys. Usp. **30**, 759 (1987)].

[22] R. Opher, Astron. Astrophys. **37**, 135 (1974); L. Stodolsky, Phys. Rev. Lett. **34**, 110 (1975); R. R. Lewis, Phys. Rev. D **21**, 663 (1980).
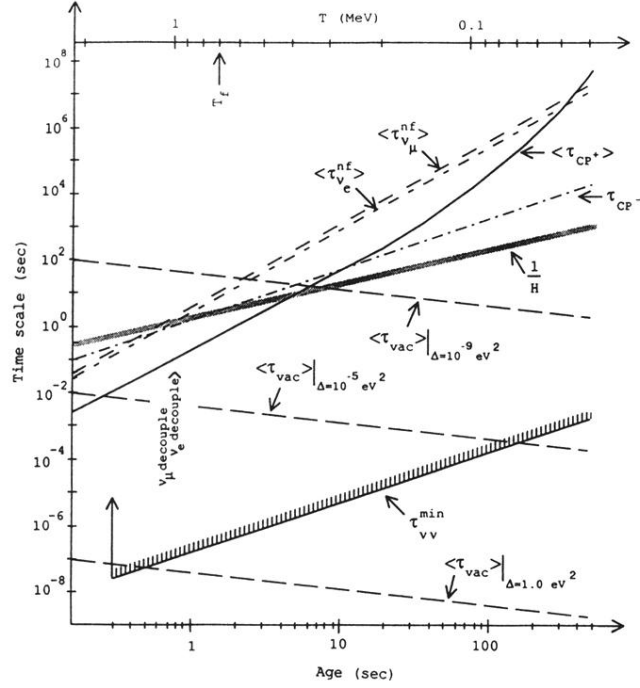
FIG. 2. Relevant time scales. Key time scales are displayed as a function of the age t of the Universe. The time scale $\langle \tau_{\text{vac}} \rangle$ is displayed for the cases $\Delta = 10^{-9}$, 10^{-5}, and 1 eV^2. For each factor of 10 increase (or decrease) in Δ, the $\langle \tau_{\text{vac}} \rangle$ line moves down (or up) by one power of ten. The $1/H$ line is drawn with width as a reminder that it acts as an order-of-magnitude estimate of the time at which a scale becomes insignificant. After the temperature of the Universe has dropped below T_f, neutrino flavor effects can no longer influence nucleosynthesis. The average nonforward scattering time scales are plotted separately for ν_e and ν_μ for an average energy of $\bar{E} = 3.151T$. The averages $\langle \tau_{CP+} \rangle$ and $\langle \tau_{\text{vac}} \rangle$ are graphed for an average energy $\bar{E} \approx 5T$. The arrow on the $\tau_{\nu\nu}^{\min}$ line indicates that this quantity becomes effectively infinite at times $t < 0.328$ s, as a result of our step-function approximation for the initial neutrino profile. The hatches on the $\tau_{\nu\nu}^{\min}$ line are a reminder that it provides a lower bound for $\tau_{\nu\nu}$.
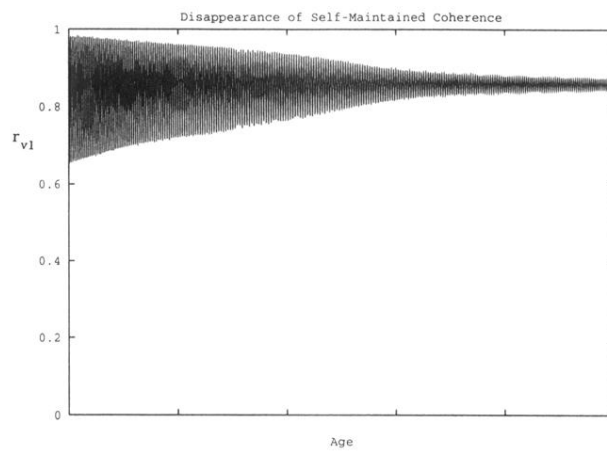
FIG. 7. Disappearance of self-maintained coherence. The small amplitude eventually shrinks to zero.